

Review

Open Access



# Recent advances and perspectives of microsized alloying-type porous anode materials in high-performance Li- and Na-ion batteries

Gaojie Li<sup>1,2,#</sup>, Siguang Guo<sup>1,#</sup>, Ben Xiang<sup>1</sup>, Shixiong Mei<sup>1</sup>, Yang Zheng<sup>1</sup>, Xuming Zhang<sup>1</sup>, Biao Gao<sup>1,\*</sup>, Paul K. Chu<sup>3</sup> , Kaifu Huo<sup>2,\*</sup> 

<sup>1</sup>The State Key Laboratory of Refractories and Metallurgy, Institute of Advanced Materials and Nanotechnology, Wuhan University of Science and Technology, Wuhan 430081, Hubei, China.

<sup>2</sup>Wuhan National Laboratory for Optoelectronics (WNLO) and School of Optical and Electronic Information, Huazhong University of Science and Technology, Wuhan 430074, Hubei, China.

<sup>3</sup>Department of Physics and Department of Materials Science and Engineering, City University of Hong Kong, Tat Chee Avenue, Kowloon, Hong Kong, China.

<sup>#</sup>Authors contributed equally.

\*Correspondence to: Prof./Dr. Biao Gao, The State Key Laboratory of Refractories and Metallurgy, Institute of Advanced Materials and Nanotechnology, Wuhan University of Science and Technology, Wuhan 430081, Hubei, China. E-mail: gaobiao@wust.edu.cn; Prof./Dr. Kaifu Huo, Wuhan National Laboratory for Optoelectronics (WNLO) and School of Optical and Electronic Information, Huazhong University of Science and Technology, Wuhan 430074, Hubei, China. E-mail: kfhuo@hust.edu.cn

**How to cite this article:** Li G, Guo S, Xiang B, Mei S, Zheng Y, Zhang X, Gao B, Chu PK, Huo K. Recent advances and perspectives of microsized alloying-type porous anode materials in high-performance Li- and Na-ion batteries. *Energy Mater* 2022;2:200020. <https://dx.doi.org/10.20517/energymater.2022.24>

**Received:** 4 May 2022 **First Decision:** 18 May 2022 **Revised:** 28 May 2022 **Accepted:** 2 Jun 2022 **Published:** 14 Jun 2022

**Academic Editors:** Yuping Wu, Bin Wang **Copy Editor:** Tiantian Shi **Production Editor:** Tiantian Shi

## Abstract

Alloying materials (e.g., Si, Ge, Sn, Sb, and so on) are promising anode materials for next-generation lithium-ion batteries (LIBs) and sodium-ion batteries (SIBs) due to their high capacity, suitable working voltage, earth abundance, environmental friendliness, and non-toxicity. Although some important breakthroughs have been reported recently for these materials, their dramatic volume change during alloying/dealloying causes severe pulverization, leading to poor cycling stability and safety risks. Although the nanoengineering of alloys can mitigate the volumetric expansion to some extent, there remain other drawbacks, such as low initial Columbic efficiency and volumetric energy density. Porous microscale alloys comprised of nanoparticles and nanopores inherit micro- and nanoproperties, so that volume expansion during lithiation/sodiation can be better accommodated by the porous structure to consequently release stress and improve the cycling stability. Herein, the recent progress of porous



© The Author(s) 2022. **Open Access** This article is licensed under a Creative Commons Attribution 4.0 International License (<https://creativecommons.org/licenses/by/4.0/>), which permits unrestricted use, sharing, adaptation, distribution and reproduction in any medium or format, for any purpose, even commercially, as long as you give appropriate credit to the original author(s) and the source, provide a link to the Creative Commons license, and indicate if changes were made.



microscale alloying-type anode materials for LIBs and SIBs is reviewed by summarizing the Li and Na storage mechanisms, the challenges associated with different materials, common fabrication methods, and the relationship between the structure and electrochemical properties in LIBs and SIBs. Finally, the prospects of porous microscale alloys are discussed to provide guidance for future research and the commercial development of anode materials for LIBs and SIBs.

**Keywords:** Alloy-type materials, microsized porous materials, lithium-ion batteries, sodium-ion batteries

## INTRODUCTION

Environmental pollution from the increasing demand for energy and the use of fossil fuels is attracting enormous attention<sup>[1,2]</sup>, and the development of green and renewable energy sources is therefore urgently required. High-performance energy storage devices are crucial to clean energy because of their special functions, such as the peak load regulation of electricity grids, electric vehicles, and mobile electronics<sup>[1,3]</sup>. Batteries composed of alkaline and alkaline earth elements (e.g., Li, Na, K, Mg, Ca, and so on) are now ubiquitous because of their high energy densities, suitable working potentials, good cycling stability, and environmental friendliness. Among them, lithium-ion batteries (LIBs) and sodium-ion batteries (SIBs) are the most widely used. A battery comprises the cathode, anode, electrolyte, and separator<sup>[4,5]</sup>, and the electrode materials are the core of the battery and determine the energy density<sup>[6-9]</sup>. However, the theoretical capacity of the aforementioned cathode materials is relatively low, resulting in low energy densities in LIBs and SIBs<sup>[10]</sup>.

Compared to cathode materials, the anode materials in LIBs or SIBs have greater potential for attaining higher energy densities because of their diversity and high theoretical capacity. The emerging anode materials can be categorized into three types according to their reaction mechanisms with Li and Na ions, namely, intercalation, conversion, and alloying<sup>[11,12]</sup>. Currently, the most extensively used LIB anode material is intercalating graphite with a theoretical specific capacity of 372 mAh g<sup>-1</sup><sup>[13]</sup>; however, it only delivers a reversible capacity of 35 mAh g<sup>-1</sup> in SIBs because of the insufficient interlayer space<sup>[14,15]</sup>. Hard carbon derived from biomass or other organic precursors with a larger disordered layer distance can store extra Na ions, but the capacity is still far from satisfactory. Furthermore, the reaction potential of carbonaceous anodes with Li and Na is relatively low, thus leading to the dendritic deposition of Li and Na metals in the electrochemical process and safety issues<sup>[16]</sup>. Conversion-type anode materials mainly consist of transition metal oxides<sup>[17]</sup>, sulfides<sup>[18-21]</sup>, selenides<sup>[22]</sup> and phosphides. Although conversion-type compounds have higher specific capacities than carbonaceous anodes, they are still plagued by low conductivity and appreciable irreversible capacities<sup>[23,24]</sup>. Different from intercalation- and conversion-type anodes, alloying materials react with Li and Na ions to form alloys, giving rise to higher theoretical capacities, larger molar ratios, safer potentials, and lower costs [Figure 1A-C] and have thus received immense attention for LIBs and SIBs.

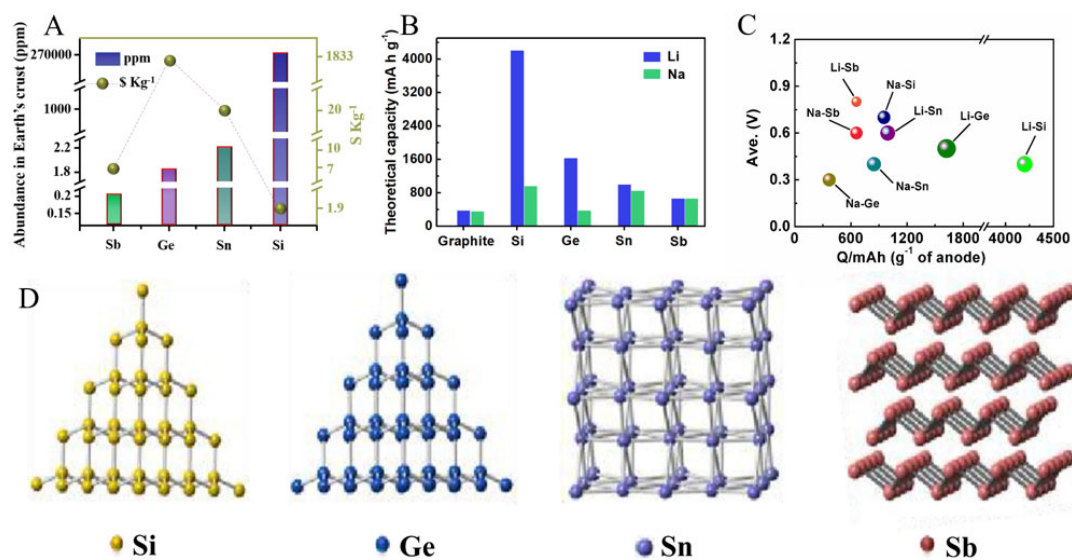
Currently, alloys containing Si, Ge, Sn, and Sb are desirable anode materials for LIBs and SIBs [Tables 1-2]. As shown in Figure 1D, Si and Ge have a diamond structure that provides space to accommodate Li<sup>+</sup> and Na<sup>+</sup> ions. Sn has a cubic structure and can also hold more Li<sup>+</sup> and Na<sup>+</sup>. In comparison, Sb has a puckered layered structure and the interlamellar spacing can effectively accommodate the insertion and alloying of Li and Na. The electrochemical reaction of alloys is as follows:  $x\text{Li} + \text{M} = \text{Li}_x\text{M}$  or  $x\text{Na} + \text{M} = \text{Na}_x\text{M}$  (M = Si, Ge, Sn, Sb, and so on), which is different from insertion/desertion in carbon-based anodes. However, the alloying reaction results in a serious volume expansion and internal stress, leading to serious pulverization of the electrode materials [Figure 2A]. The frequent volumetric change during cycling also results in repeated formation and destruction of the solid electrolyte interface (SEI), which is the

**Table 1. Electrochemical parameters of major alloying-type anode materials for LIBs**

Element	Alloying product	Theoretical capacity (mAh g <sup>-1</sup> )	Volumetric capacity (mAh cm <sup>-3</sup> )	Volume expansion ratio (%)	Conductivity (S m <sup>-1</sup> )	Density (g cm <sup>-3</sup> )
Si	Li <sub>22</sub> Si <sub>5</sub>	4200	2190	> 300	2.52 × 10 <sup>4</sup>	2.35
Ge	Li <sub>22</sub> Ge <sub>5</sub>	1624	2180	370	2.17	5.35
Sn	Li <sub>22</sub> Sn <sub>5</sub>	994	1991	340	9.09 × 10 <sup>6</sup>	7.28
Sb	Li <sub>3</sub> Sb	660	1889	200	2.45 × 10 <sup>6</sup>	6.68

**Table 2. Electrochemical parameters of major alloying-type anode materials for SIBs**

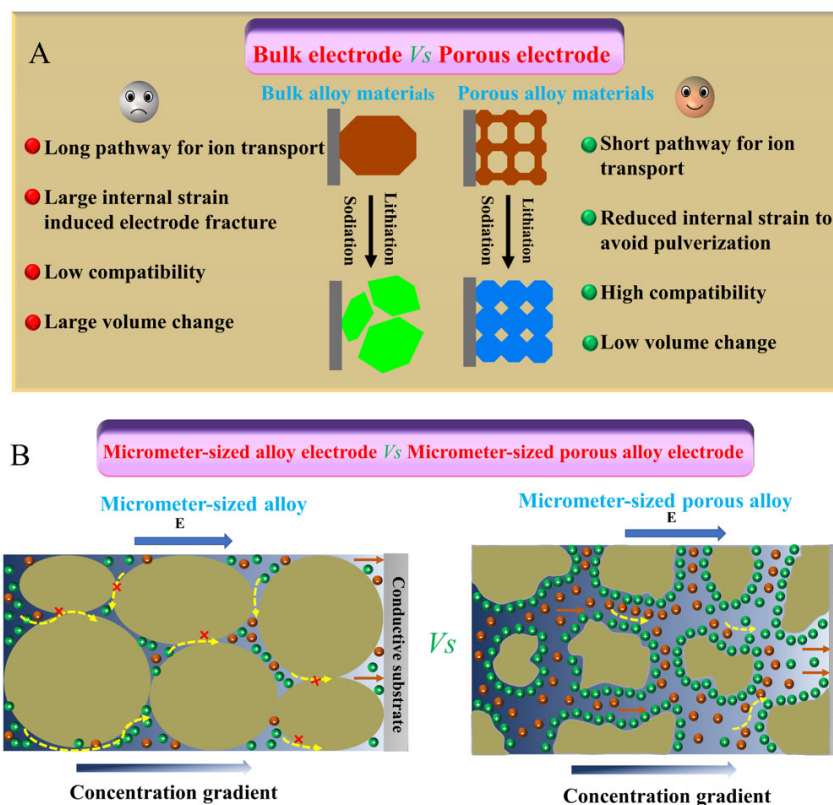
Element	Alloying product	Theoretical capacity (mAh g <sup>-1</sup> )	Volumetric capacity (mAh cm <sup>-3</sup> )	Volume expansion ratio (%)	Conductivity (S m <sup>-1</sup> )	Density (g cm <sup>-3</sup> )
Si	NaSi	954	2190	> 244	2.52 × 10 <sup>4</sup>	2.35
Ge	NaGe	369	2180	300	2.17	5.35
Sn	Na <sub>15</sub> Sn <sub>4</sub>	847	1991	525	9.09 × 10 <sup>6</sup>	7.28
Sb	Na <sub>3</sub> Sb	660	1889	390	2.45 × 10 <sup>6</sup>	6.68



**Figure 1.** (A) Crustal abundance (ppm) and cost of alloying-type anodes (data for Sb, Ge, Sn, and Si costs taken from Shanghai Metals Market, Kitco Metals, London metal exchange, and Deutsche Rohstoffagentur, respectively). (B) Theoretical lithiation capacities of graphite, Si, Ge, and Sn for LIBs and SIBs. (C) Average potential of various alloy materials in LIBs and SIBs. (D) Crystal structures of Si, Ge, Sn, and Sb.

main reason for fast electrolyte consumption and capacity degradation<sup>[25,26]</sup>. Moreover, some nonmetallic alloys composed of Si and P show relatively low conductivity and poor rates.

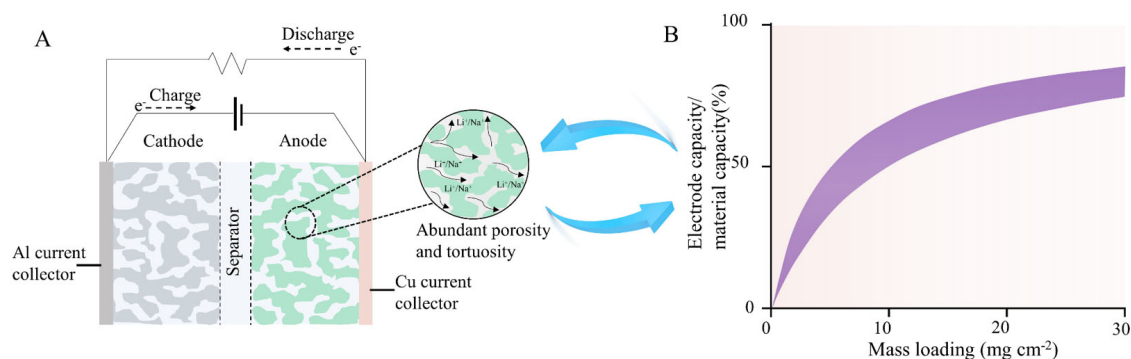
To address the issues of bulk alloying materials, nanoengineering is adopted to increase the active sites, decrease the Li- and Na-ion diffusion distance, and mitigate the volume expansion and resulting stress<sup>[27]</sup>. Nanostructured alloys can be endowed with high gravimetric capacities and rates and superior fracture toughness. However, because of the large specific Brunner-Emmet-Teller (BET) surface, low tap density, and complex fabrication process, some obstacles, such as the low initial Coulombic efficiency (ICE), inferior volumetric capacity, and high manufacturing costs, hinder the development and subsequent replacement for traditional electrode materials. Nevertheless, research into microscale alloying anode material continues



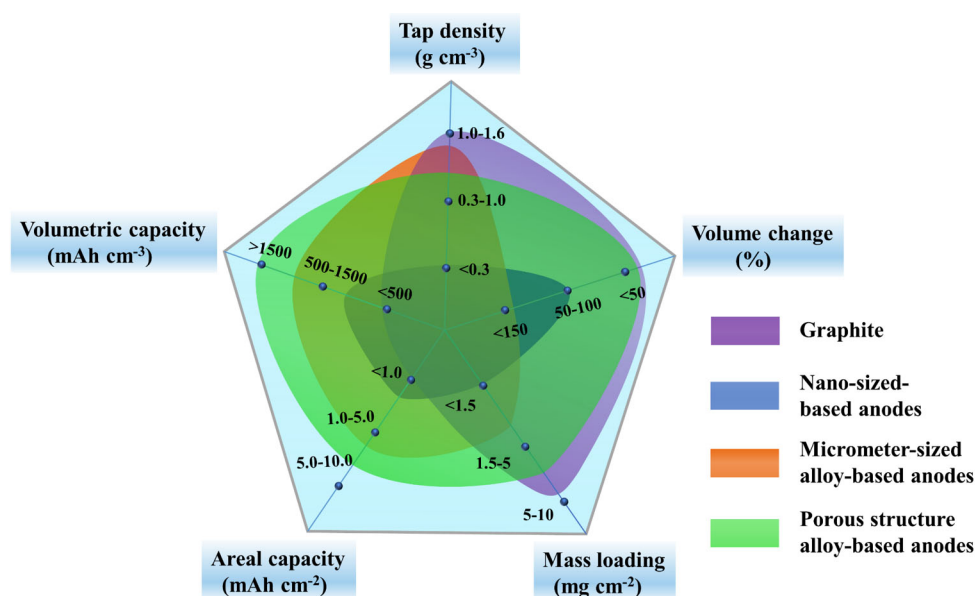
**Figure 2.** (A) Overview of bulk electrode and porous alloy-based anode materials. (B) Structural design for electrodes comprised of alloying-type anode materials.

because compared to nanoscale materials, they have higher ICE, volumetric capacity, and mass loading due to the high tap density and small BET surface. However, microscale alloys with large particle sizes have drawbacks, such as large ion and electron diffusion distances, pulverization, large volumetric expansion, and poor rates [Figure 2B]. Ideal alloying-type anode materials should combine the advantages of both nano- and microscale materials by incorporating an overall microscale morphology and built-in nanoscale features.

On this basis, porous microscale materials consisting of nanoblocks and nanopores have aroused significant interest as a result of the following metrics<sup>[28]</sup>. First, alloys with controllable porosity and pore size can accommodate the volume change during lithiation/sodiation and decrease the volume expansion at the particle level [Figure 2A]. The smaller volume change further impedes the swelling of the electrode and disconnection of the active materials from the current collector. Second, the porous structure enhances electrolyte infiltration, reduces the ion/electron transfer distance, and decreases the internal impedance of the electrode to improve the kinetics [Figure 3A]. Third, they have a high tap density and small specific BET surface area, leading to a high ICE, mass loading, and energy density. In addition, microsized porous materials show obvious advantages in mass transfer because of the three-dimensional (3D) electrolyte permeating channels. Therefore, microsized alloying materials may show utilization even at a mass loading of the active materials [Figure 3B]. Fourth, the interconnected pores offer more active sites for a higher capacity. In general, porous microscale alloys containing nanoparticles deliver better comprehensive performance than either nano- or microscale alloys in LIBs and SIBs [Figure 4].



**Figure 3.** (A) Basic configuration and working mechanism of a cell. A typical battery device consists of a porous anode and a cathode film sandwiched between two current collectors and isolated by an insulating separator. (B) Plot showing that the capacity of an electrode is positively proportional to the mass loading of active materials on it<sup>[4]</sup> (Copyright 2017, The American Association for the Advancement of Science).



**Figure 4.** Comparison of critical practical metrics required for commercial LIB anodes.

Alloys are promising materials in rechargeable Li-, Na-, Mg- and K-ion batteries because of their high theoretic capacity. To overcome the intrinsic problems of such alloys, including the large volumetric expansion and unstable interfaces, nanoengineering and their combination with carbonaceous materials are two major strategies that have been summarized in recent reviews<sup>[29-33]</sup>. Porous microscale particles with engineered nano-units and nanoporosity enable relatively stable cycling and low volumetric expansion. However, reviews focusing on these materials for advanced batteries are scarce, and a timely and comprehensive review to facilitate future development is still lacking. This review summarizes the recent development of porous microscale alloying anode materials for LIBs and SIBs. First, the structural design and fabrication methods are described. Focus is given to materials containing continuous nano-units and adjacent nanopores to take advantage of the merits of nanoscale materials, such as the high activity and small ion diffusion distance, as well as microscale materials, including the high tap density and ICE. Representative alloys consisting of Si, Ge, Sn, and Sb and their electrochemical properties in LIBs and SIBs are described, and their future directions and prospects are discussed. This review offers a critical summary



of recent advances in the field and will spur the future development of high-efficiency energy storage devices.

## SYNTHETIC METHODOLOGIES OF MICROSIZED POROUS ALLOYING MATERIALS

The controllable synthesis of porous alloying microscale materials consisting of nano-ligaments and surrounding nanopores has been reported. In this section, the fabrication protocols are described, and Tables 3-5 summarize the various preparation techniques, including dealloying, templating, chemical etching, and self-assembly.

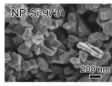

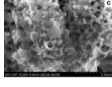
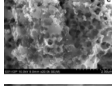
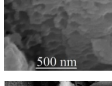
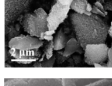
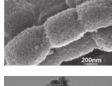
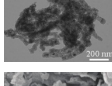
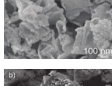
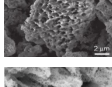
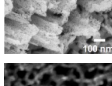
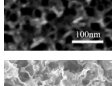
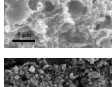
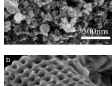
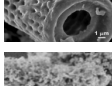
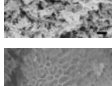
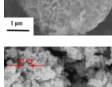

### Dealloying methods

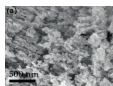
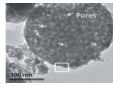
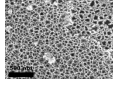
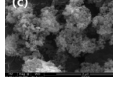
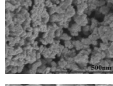
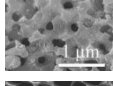
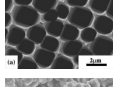
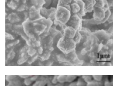
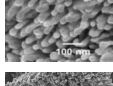
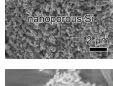
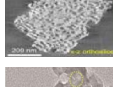
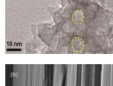

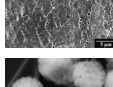
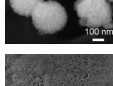
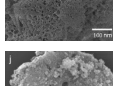
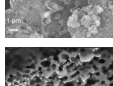
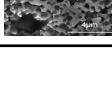
Dealloying is often expressed as a bimetallic or multi-metal alloy corrosion process, in which more active metals in the precursors react selectively with the medium and are removed *operando* in the following steps to leave a more stable component. During the reaction, the residual component diffuses between the parent alloy and reactive medium to form a bicontinuous porous structure with 3D open pores and maximum interfaces<sup>[34]</sup>. Dealloying has attracted intensive attention for the fabrication of porous alloys because pore creation does not require additives and adjustable structures. The 3D porous alloying metal supplies rich Li and Na storage and active sites and enables rapid mass transfer, which is vital for LIBs and SIBs. According to different alloy precursors, the porosity of the structure can be adjusted from 40% to 80% by taking advantage of the alloy parting limit<sup>[34,35]</sup>. The dealloying of porous structures is carried out by chemical, electrochemical, low-melting metal, and other dealloying methods.

Chemical dealloying is one of the most common methods to obtain porous structures from the alloy precursor via spontaneous chemical reactions based on the different standard electrode potentials in an acidic or alkaline solution. The precursor alloy must be homogeneous or have an intermetallic phase comprising a relatively active metal and another more inert one. Porous metals containing Si, Ge, Sn, Sb, and so on have been prepared by dealloying routes. For example, Feng *et al.* fabricated porous Si consisting of nanodendrites by direct dealloying of a commercial Al-Si eutectic alloy with microparticles in 5 M HCl for 24 h<sup>[36]</sup>. Zhang *et al.* prepared porous microscale antimony from Mg-Sb alloys by one-step chemical vapor dealloying with a HCl vapor as the dissolution medium at 600 °C [Figure 5A]<sup>[37]</sup>. Sohn *et al.* prepared porous Si via the dealloying of Si/Al-Cu-Fe nanoparticles obtained from smelting, roller melt-spinning, and attrition milling via dual-step acidic and alkaline wet chemical etching<sup>[38]</sup>. Lin *et al.* reported a low-temperature molten salt system for the metallothermic (Mg or Zn) reduction of GeO<sub>2</sub> to obtain mesoporous hollow Ge microspheres, and the molten ZnCl<sub>2</sub> promotes the reaction at a low temperature. In the etching process, part of the metal alloy matrix is consumed due to acid leaching to generate abundant pores, and subsequent alkaline etching decreases the Si domain size and enlarges the pores<sup>[39]</sup>.

In addition to single metals, porous bimetallic materials have also been obtained by chemical dealloying using ternary alloys as the raw materials. Yang *et al.* produced Si-Ge bimetallic porous materials via the dealloying of Al-Ge-Si microparticles with an Al content of 80% in HCl<sup>[40]</sup>. Other bimetallic compounds, such as Bi-Sn<sup>[41]</sup>, Ag-Ge<sup>[42]</sup>, SnSb<sup>[43]</sup>, and SnNi<sup>[44]</sup>, have been formed by similar dealloying methods. Although chemical dealloying using acidic and alkaline media as the dissolving agents is an emerging route, there are some shortcomings, such as its time-consuming nature, the production of waste acidic or alkaline solutions, and structural collapse of the porous architecture. To solve these problems, electrochemical dealloying methods have been developed to obtain porous Si, Ge, and Ge-Si alloys by adjusting the applied potential. Yin *et al.* conducted electrochemical dealloying in a molten CaCl<sub>2</sub>-NaCl eutectic electrolyte at 600 °C to produce porous Ge<sup>[45]</sup>. Yuan *et al.* adopted Mg alloying/dealloying using a molten MgCl<sub>2</sub>-NaCl-KCl electrolyte at 500 °C to fabricate porous Si<sup>[46]</sup>. Although the porous structure can be retained, the conditions

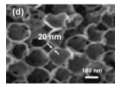
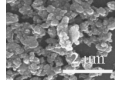
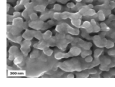
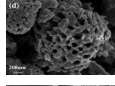
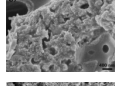
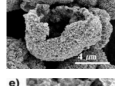
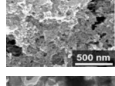
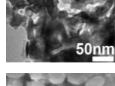
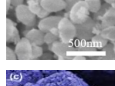
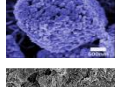
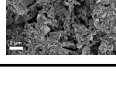
**Table 3. Synthesis strategies and electrochemical properties of porous Si electrode in LIBs**

Structures	Method	Morphology	Initial capacity	ICE	Capacity retention	Reference
<b>NP-Si</b>	Dealloying in metallic melt		3,200 mAh g <sup>-1</sup> at 4.2 A g <sup>-1</sup>	77%	2,100 mAh g <sup>-1</sup> after 100 cycles at 4.2 A g <sup>-1</sup>	[48]
<b>3D porous Si</b>	Wet alkaline chemical etching		2,919 mAh g <sup>-1</sup> at 0.5 A g <sup>-1</sup>	76.5%	1,222 mAh g <sup>-1</sup> after 200 cycles at 500 mA g <sup>-1</sup>	[38]
<b>Porous Si</b>	Magnesiothermic reduced		1,321 mAh g <sup>-1</sup> at 0.2 mA cm <sup>-2</sup>	72.7%	633 mAh g <sup>-1</sup> after 30 cycles at 0.2 mA cm <sup>-2</sup>	[94]
<b>MP-Si</b>	Magnesiothermic reduction		2,638.3 mAh g <sup>-1</sup> at 0.1 A g <sup>-1</sup>	85.1%	1,000 mAh g <sup>-1</sup> after 360 cycles at 500 mA g <sup>-1</sup>	[95]
<b>Porous Si</b>	Ball-milling and acid etching		1,957.6 mAh g <sup>-1</sup> at 50 mA g <sup>-1</sup>	88.1%	1,250 mAh g <sup>-1</sup> after 100 cycles at 500 mA g <sup>-1</sup>	[96]
<b>Bulk porous Si</b>	Cu-assisted etching method		2,126 mAh g <sup>-1</sup> at 0.2 A g <sup>-1</sup>	92%	1,938.3 mAh g <sup>-1</sup> after 50 cycles at 200 A g <sup>-1</sup>	[97]
<b>3D mp-Si</b>	Template method		1,945 mAh g <sup>-1</sup> at 0.84 A g <sup>-1</sup>	73.6%	1,500 mAh g <sup>-1</sup> after 100 cycles at 4.2 A g <sup>-1</sup>	[98]
<b>Mesoporous Si</b>	Template method		1,586 mAh g <sup>-1</sup> at 0.2 A g <sup>-1</sup>	48.3%	1,038 mAh g <sup>-1</sup> after 170 cycles at 200 mA g <sup>-1</sup>	[99]
<b>Porous Si nanosheets</b>	Template method		2,551.5 mAh g <sup>-1</sup> at 240 mA g <sup>-1</sup>	74%	800 mAh g <sup>-1</sup> after 900 cycles at 8,400 mA g <sup>-1</sup>	[100]
<b>3D porous Si</b>	Metal assisted chemical etching		2,390 mAh g <sup>-1</sup> at 0.2 A g <sup>-1</sup>	94.4%	2,079.3 mAh g <sup>-1</sup> after 200 cycles at 0.4 A g <sup>-1</sup>	[101]
<b>MG-SiNWs</b>	Metal-assisted chemical etching		2,111 mAh g <sup>-1</sup> at 0.84 A g <sup>-1</sup>	52.8%	2,111 mAh g <sup>-1</sup> after 50 cycles at 0.84 A g <sup>-1</sup>	[72]
<b>Mesoporous Si sponge</b>	Electrochemical etching		750 mAh g <sup>-1</sup> at 0.1 A g <sup>-1</sup>	156%	640 mAh g <sup>-1</sup> after 1,000 cycles at 1 A g <sup>-1</sup>	[102]
<b>Porous Si</b>	Cu-assisted chemical etching		1,521.9 mAh g <sup>-1</sup> at 50 mA g <sup>-1</sup>	57.5%	996.5 mAh g <sup>-1</sup> after 100 cycles at 50 mA g <sup>-1</sup>	[103]
<b>Mesoporous Si</b>	Magnesium thermal		1,216 mAh g <sup>-1</sup> at 400 mA g <sup>-1</sup>	66%	1,400 mAh g <sup>-1</sup> after 100 cycles at 400 mA g <sup>-1</sup>	[104]
<b>Macroporous Si</b>	Aluminothermic reduction		3,385 mAh g <sup>-1</sup> at 0.21 A g <sup>-1</sup>	86.7%	1,500 mAh g <sup>-1</sup> after 100 cycles at 0.84 A g <sup>-1</sup>	[105]
<b>Nanoporous Si</b>	Air-Oxidation Demagnesian		3,291 mAh g <sup>-1</sup> at 0.36 A g <sup>-1</sup>	88%	1,200 mAh g <sup>-1</sup> after 400 cycles at 1.8 A g <sup>-1</sup>	[106]
<b>Nanoporous Si</b>	HCl etching		2,244 mAh g <sup>-1</sup> at 0.06 A g <sup>-1</sup>	86%	1,400 mAh g <sup>-1</sup> after 60 cycles at 0.24 A g <sup>-1</sup>	[107]
<b>Porous Si</b>	Magnesiothermic reduction		1,731 mAh g <sup>-1</sup> at 0.1 A g <sup>-1</sup>	64.8%	1,030 mAh g <sup>-1</sup> after 300 cycles at 1 A g <sup>-1</sup>	[108]

<b>Porous Si</b>	Solvothermal reaction		1,679 mAh g <sup>-1</sup> at 0.5 A g <sup>-1</sup>	64.6%	1,025 mAh g <sup>-1</sup> after 700 cycles at 3 A g <sup>-1</sup>	[109]
<b>Mesoporous Si</b>	Magnesiothermic reduction		830 mAh g <sup>-1</sup> at 0.5 A g <sup>-1</sup>	87%	1,199 mAh g <sup>-1</sup> after 500 cycles at 0.5 A g <sup>-1</sup>	[110]
<b>Porous Si</b>	Electrochemical etching		2,073 mAh g <sup>-1</sup> at 4.2 A g <sup>-1</sup>	92%	1,453.5 mAh g <sup>-1</sup> after 100 cycles at 4.2 A g <sup>-1</sup>	[111]
<b>Mesoporous Si</b>	Zeolite-templated		1,184 mAh g <sup>-1</sup> at 0.1 A g <sup>-1</sup>	73.1%	888 mAh g <sup>-1</sup> after 300 cycles at 1 A g <sup>-1</sup>	[112]
<b>Porous Si</b>	Acidic ionic liquid		2,036 mAh g <sup>-1</sup> at 0.1 A g <sup>-1</sup>	72.9%	1,000 mAh g <sup>-1</sup> after 100 cycles at 1 A g <sup>-1</sup>	[113]
<b>Porous Si spheres</b>	Magnesiothermic reduction		3,191 mAh g <sup>-1</sup> at 0.42 A g <sup>-1</sup>	80.9%	1,620 mAh g <sup>-1</sup> after 20 cycles at 420 mA g <sup>-1</sup>	[114]
<b>Macroporous Si</b>	Electrochemical anodization		1,425 mAh g <sup>-1</sup> at 0.04 A g <sup>-1</sup>	81%	600 mAh g <sup>-1</sup> after 20 cycles at 200 mA g <sup>-1</sup>	[115]
<b>Porous Si</b>	Heat-treated and HCl etching		2,182 mAh g <sup>-1</sup> at 0.1 A g <sup>-1</sup>	71.4%	750 mAh g <sup>-1</sup> after 250 cycles at 2 A g <sup>-1</sup>	[116]
<b>nSi</b>	Electrochemical Mg dealloying		2,920 mAh g <sup>-1</sup> at 1 A g <sup>-1</sup>	90%	1,430 mAh g <sup>-1</sup> after 300 cycles at 3 A g <sup>-1</sup>	[46]
<b>NP-Si</b>	Mg-Bi-Si dealloying		3,500 mAh g <sup>-1</sup> at 2.1 A g <sup>-1</sup>	85%	2,000 mAh g <sup>-1</sup> after 150 cycles at 2.1 A g <sup>-1</sup>	[117]
<b>Porous Si</b>	Ball-milling and stain-etching		2,900 mAh g <sup>-1</sup> at 0.42 A g <sup>-1</sup>	83%	1,100 mAh g <sup>-1</sup> after 600 cycles at 2.1 A g <sup>-1</sup>	[118]
<b>Porous Si</b>	Magnesiothermic reaction		1,045.6 mAh g <sup>-1</sup> at 1 A g <sup>-1</sup>	68.2%	697.7 mAh g <sup>-1</sup> after 200 cycles at 1 A g <sup>-1</sup>	[119]
<b>1D-PSiNW</b>	Metal assisted chemical etching		2,534.5 mAh g <sup>-1</sup> at 1 A g <sup>-1</sup>	56.5%	586.7 mAh g <sup>-1</sup> after 5,000 cycles at 16 A g <sup>-1</sup>	[120]
<b>Porous Si</b>	Fe-Si dealloying		3,185 mAh g <sup>-1</sup> at 50 mA g <sup>-1</sup>	89%	2,120 mAh g <sup>-1</sup> after 140 cycles at 0.5 A g <sup>-1</sup>	[121]
<b>Porous Si spheres</b>	Magnesiothermic reduction		3,105 mAh g <sup>-1</sup> at 0.21 A g <sup>-1</sup>	64%	1,500 mAh g <sup>-1</sup> after 500 cycles at 2.1 A g <sup>-1</sup>	[122]
<b>Porous Si</b>	Al-Si dealloying		2,606 mAh g <sup>-1</sup> at 0.53 A g <sup>-1</sup>	76.7%	1,000 mAh g <sup>-1</sup> after 300 cycles at 1.4 A g <sup>-1</sup>	[123]
<b>Mesoporous Si</b>	Self-assembly methods		1,917.2 mAh g <sup>-1</sup> at 20 mA g <sup>-1</sup>	69.9%	1,147.7 mAh g <sup>-1</sup> after 100 cycles at 0.2 A g <sup>-1</sup>	[88]
<b>Mesoporous Si</b>	Magnesiothermic reduction		1,300 mAh g <sup>-1</sup> at 100 mA g <sup>-1</sup>	75%	1,053 mAh g <sup>-1</sup> after 100 cycles at 0.1 A g <sup>-1</sup>	[124]



**Table 4. Synthesis strategies and electrochemical properties of porous Ge electrodes in LIBs**

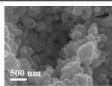
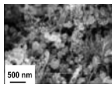
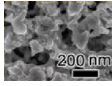

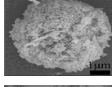
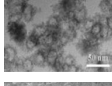
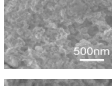
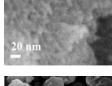
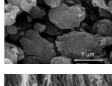
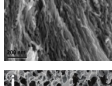
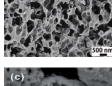
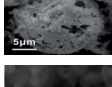

Structures	Method	Morphology	Initial capacity	ICE	Capacity retention	Reference
<b>3D Porous Ge</b>	Etching SiO <sub>2</sub> template		1,380 mAh g <sup>-1</sup> at 0.5C	90%	1,415 mAh g <sup>-1</sup> after 100 cycles at 1C	[141]
<b>Mesoporous Ge</b>	Mechanochemical reaction		944 mAh g <sup>-1</sup> at 0.1C	43.8%	789 mAh g <sup>-1</sup> after 20 cycles at 0.1C	[142]
<b>Porous Ge</b>	Self-assembled		1,450 mAh g <sup>-1</sup> at 0.03C	75.5%	1,500 mAh g <sup>-1</sup> after 40 cycles at 0.3C	[143]
<b>Microporous Ge</b>	Magnesiothermic reduction		1,299 mAh g <sup>-1</sup> at 0.1C	80.3%	1,131 mAh g <sup>-1</sup> after 200 cycles at 1C	[63]
<b>Macro-Ge</b>	Hydrothermal reduction		1,263 mAh g <sup>-1</sup> at 0.2C	84%	755 mAh g <sup>-1</sup> after 3,500 cycles at 1C	[144]
<b>Meso-porous Ge</b>	Metallothermal reduction		1,340 mAh g <sup>-1</sup> at 0.2C	65.5%	1,217 mAh g <sup>-1</sup> after 400 cycles at 0.8C	[39]
<b>3D-pGe</b>	Hydrogen reduction		1,341.1 mAh g <sup>-1</sup> at C/20	92.3%	770 mAh g <sup>-1</sup> after 250 cycles at 1C	[145]
<b>Porous Ge</b>	Modified Stöber method		1,568 mAh g <sup>-1</sup> at C/20	85.3%	1,140 mAh g <sup>-1</sup> after 300 cycles at 0.5C	[146]
<b>Mesoporous Ge</b>	Redox transmetalation reaction		1,585 mAh g <sup>-1</sup> at 0.05C	89%	1,400 mAh g <sup>-1</sup> after 300 cycles at 0.5C	[147]
<b>Ge microcubes</b>	Hydrogen reaction		1,275 mAh g <sup>-1</sup> at 0.1C	91.8%	1,204 mAh g <sup>-1</sup> after 500 cycles at 1C	[148]
<b>Mesoporous Ge</b>	Metathesis reaction		1,479.5 mAh g <sup>-1</sup> at 0.2C	80.4%	1,048 mAh g <sup>-1</sup> after 1,000 cycles at 1.0C	[149]

in electrochemical dealloying are relatively harsh and an oxygen-free environment is needed to prevent oxidation of the porous materials.

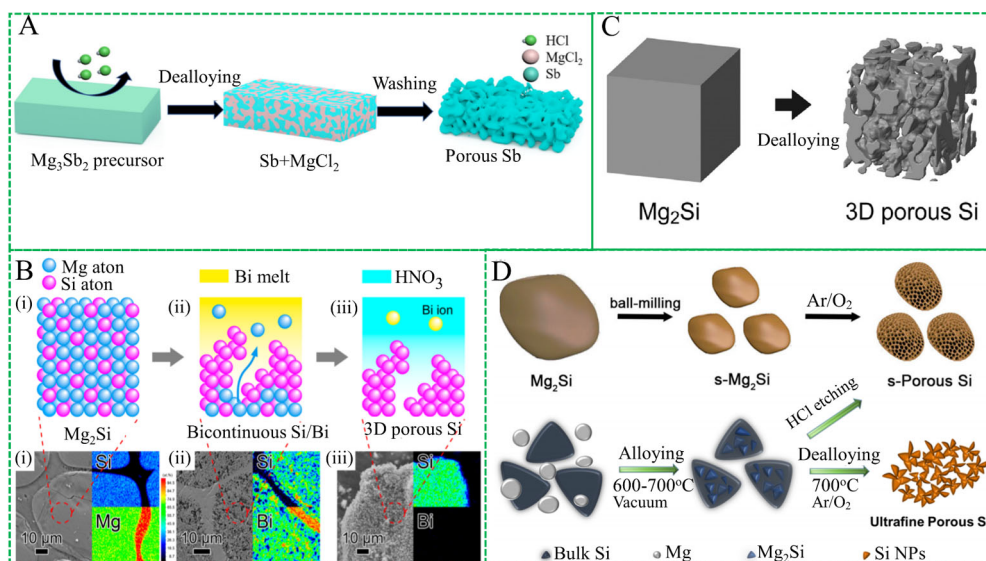
Liquid metal dealloying has been proposed to prepare porous alloys because of the controllable porosity. Wada *et al.* reported the fabrication of bulk 3D porous Si via a metallic melting dealloying route with Mg<sub>2</sub>Si as the precursor and Bi metal as the dealloying melting medium<sup>[47]</sup>. Mg dissolves selectively from the Si-Mg alloy into the Bi melt to produce porous Si at high temperatures [Figure 5B]. Similarly, Wada *et al.* fabricated porous 3D Si by immersing a Mg-Si alloy precursor in a Bi melt and washing it with 1 M nitric acid [Figure 5C]<sup>[48]</sup>. However, electrochemical and melting metal dealloying have some disadvantages, including environmental issues and economic efficiency, which hinder their wider application.

Alternative dealloying methods have been developed to obtain more desirable porous structures efficiently. For instance, Chen *et al.* and Wang *et al.* synthesized porous Si structures with various particle sizes *via* the oxidation of ball-milled Mg<sub>2</sub>Si in Ar/O<sub>2</sub> or air in conjunction with pickling reactions in HCl to remove the MgO impurity [Figure 5D]<sup>[49,50]</sup>. We recently developed a new strategy to fabricate ant-nest-like nanoporous Si microparticles by nitriding Mg<sub>2</sub>Si particles under nitrogen at 750 °C to generate a Mg<sub>3</sub>N<sub>2</sub>/Si composite,

**Table 5. Synthesis strategies and electrochemical properties of porous Sn and Sb electrode in SIBs**

Structures	Method	Morphology	Initial capacity	ICE	Capacity retention	Reference
<b>Porous Sn</b>	Dealloying		500 mAh g <sup>-1</sup> at 40 mA g <sup>-1</sup>	90.9%	275 mAh g <sup>-1</sup> after 95 cycles at 40 mA g <sup>-1</sup>	[166]
<b>Porous Sn</b>	Phase-inversion technique		674 mAh g <sup>-1</sup> at 423.5 mA g <sup>-1</sup>	63%	519 mAh g <sup>-1</sup> after 500 cycles at 423.5 mA g <sup>-1</sup>	[161]
<b>3D porous Sn</b>	Replacement reaction		823 mAh g <sup>-1</sup> at 200 mA g <sup>-1</sup>		700 mAh g <sup>-1</sup> after 400 cycles at 2.5A g <sup>-1</sup>	[162]
<b>Microsized Sn</b>	Ball-milled		847 mAh g <sup>-1</sup> at 0.847 A g <sup>-1</sup>	92%	768 mAh g <sup>-1</sup> after 100 cycles at 0.25A g <sup>-1</sup>	[164]
<b>Porous Sn</b>	Galvanic replacement reaction		1,100 mAh g <sup>-1</sup> at 0.1A g <sup>-1</sup>	69%	480.8 mAh g <sup>-1</sup> after 100 cycles at 1A g <sup>-1</sup>	[167]
<b>Hollow Sn</b>	Solution-based reduction		680 mAh g <sup>-1</sup> at 20 mA g <sup>-1</sup>	78.5%	220 mAh g <sup>-1</sup> after 50 cycles at 20 mA g <sup>-1</sup>	[168]
<b>Porous Sb</b>	Magnesiothermic reduction		570.3 mAh g <sup>-1</sup> at 50 mA g <sup>-1</sup>	81.4%	538 mAh g <sup>-1</sup> after 50 cycles at 50 mA g <sup>-1</sup>	[169]
<b>Porous Sb</b>	Sb-Mn dealloying		545 mAh g <sup>-1</sup> at 66 mA g <sup>-1</sup>		541 mAh g <sup>-1</sup> after 200 cycles at 330 mA g <sup>-1</sup>	[170]
<b>Porous Sb/C</b>	Ball-milling		480 mAh g <sup>-1</sup> at 0.1A g <sup>-1</sup>		283 mAh g <sup>-1</sup> after 3,000 cycles at 5.0 A g <sup>-1</sup>	[171]
<b>Mesoporous Sb</b>	Mg-Sb dealloying		640 mAh g <sup>-1</sup> at 0.2 A g <sup>-1</sup>	67.9%	658 mAh g <sup>-1</sup> after 200 cycles at 0.2 A g <sup>-1</sup>	[172]
<b>NP-Sb70</b>	Chemically etching		420 mAh g <sup>-1</sup> at 3.3 A g <sup>-1</sup>		573.8 mAh g <sup>-1</sup> after 200 cycles at 1.0 A g <sup>-1</sup>	[173]
<b>Sb porous microspheres</b>	Templates method		634.6 mAh g <sup>-1</sup> at 0.1 A g <sup>-1</sup>	64.6%	617 mAh g <sup>-1</sup> after 100 cycles at 1.0 A g <sup>-1</sup>	[174]
<b>Sb hollow spheres</b>	Galvanic replacement		603.5 mAh g <sup>-1</sup> at 50 mA g <sup>-1</sup>	77%	622.2 mAh g <sup>-1</sup> after 50 cycles at 50 mA g <sup>-1</sup>	[175]

followed by the dissolution of Mg<sub>3</sub>N<sub>2</sub> in HCl. The ant-nest-like porous Si comprises 3D-interconnected Si nano-ligaments and bicontinuous nanopores<sup>[51]</sup>. More recently, An *et al.* fabricated uniform porous Si particles by treating a commercial Mg-Si alloy in CO<sub>2</sub> at 500-700 °C and etching MgO in HCl<sup>[52]</sup>. In this process, CO<sub>2</sub> is reduced into the carbon layer, which is *in situ* coated on the surface of porous Si. The gas dealloying method involving a reactive gas, such as O<sub>2</sub>, N<sub>2</sub>, or CO<sub>2</sub>, reacting with the Si-Mg alloy produces phase separation and generates the 3D composite comprising Si nano-ligaments and the surrounding intermediate product. The porous 3D structure is obtained after dissolving the intermediate product. Compared to the chemical/electrochemical dealloying method, the gas dealloying technique not only can avoid structural collapse during etching but is also more environmentally friendly and faster.



**Figure 5.** Schematic illustrations of porous metal preparation via dealloying fabrication methods. (A) Schematic illustration of fabrication procedures of P-Sb. Reproduced with permission<sup>[37]</sup> (Copyright 2020, Elsevier B.V.). (B) Preparation of bulk 3D porous-Si by dealloying in a metallic melt. Reproduced with permission<sup>[47]</sup> (Copyright 2014, ACS Publications). (C) Schematic illustration of fabrication procedures of 3D porous Si. Reproduced with permission<sup>[48]</sup> (Copyright 2016, Elsevier B.V.). (D) Schematic illustration for the multi-step synthesis of ultrafine Si porous structures. Reproduced with permission<sup>[49]</sup> (Copyright 2020, Kluwer Academic Publishers).

### Template method

The template method is one of the most common methods to construct porous materials because the product has the inverse structure of the porous template. Moreover, the size of the porous structure can be adjusted by controlling the template parameters. The common templates are opals, organic spheres, and SiO<sub>2</sub>. The template method proceeds by the following steps. Infiltration of the precursor by chemical vapor deposition (CVD) or the sol-gel method is performed, followed by elimination of the matrix either by thermal annealing or chemical etching<sup>[53]</sup>. For example, Song *et al.* used silica opal as a porous template to prepare Ge inverse opal with porous walls by CVD and a Ge wall layer on the silica opal<sup>[54]</sup>. The silica template was then etched selectively with HF. Geier *et al.* produced porous Ge structures by etching and annealing the Ge precursor-loaded poly(methyl methacrylate) template<sup>[55]</sup>. The template was eliminated by heating at 500 °C for 5 min under a vacuum. In addition to Ge and Si, regular porous structures can be prepared by the deposition of a Si layer on a SiO<sub>2</sub> opal template with Si<sub>2</sub>H<sub>6</sub> as the gas precursor, followed by dissolution in HF<sup>[56]</sup>. However, in addition to the complicated preparation process and high-cost template, the template method for porous structures often involves highly toxic acids or emits a large amount of CO<sub>2</sub><sup>[57,58]</sup>.

To overcome these drawbacks, the self-template synthesis of porous materials has been developed using metal oxides, such as SiO<sub>2</sub>, GeO<sub>2</sub>, and SnO<sub>2</sub>, as both the raw materials and self-sacrificial templates<sup>[59,60]</sup>. For instance, Bao *et al.* converted microscale diatomite into porous 3D microscale Si with continuous nano-ligaments at a relatively low temperature of 650 °C by the following reaction<sup>[59]</sup>:



Some natural or synthetic porous SiO<sub>2</sub> materials, such as zeolite SSZ-13<sup>[61]</sup>, have been used in the fabrication of porous Si. The by-product of MgO is usually used as the pore-forming agent, which can generate

uniform nanoscale pores after dissolution in diluted HCl<sup>[62]</sup>. Similarly, porous Ge can be obtained by magnesiothermic reduction (MgR) with GeO<sub>2</sub> as the self-sacrificial template<sup>[63]</sup>. In addition to MgR, aluminothermic reduction in molten salt can convert the SiO<sub>2</sub> template into porous Si at a low temperature below 300 °C. For example, porous crystalline Si has been synthesized by the aluminothermic reduction of an AlCl<sub>3</sub> salt at 250 °C<sup>[64]</sup>, and other reducing agents, such as Zn and NaBH<sub>4</sub>, have been employed to convert GeO<sub>2</sub> into porous Ge<sup>[65]</sup>.

The soluble salt-template method has been developed to prepare porous alloys because the soluble salts can be easily removed. The pores are produced by removing the salt by-products of the template rather than chemical etching, thus providing both high porosity and controllability. In addition, the surface area and pore size of the materials can be adjusted by selecting appropriate alloy precursors. Some inorganic salts, such as NaCl, KCl, and LiCl, have been utilized as templates<sup>[66]</sup>. Dai *et al.* reported a bottom-up approach for mesoporous crystalline Si with tunable particle/pore size by SiCl<sub>4</sub> reduction [Figure 6A]<sup>[67]</sup>. In this process, SiCl<sub>4</sub> is the Si precursor and NaK is the reducing agent. Si and the salt by-products (NaCl and KCl) are considered to precipitate simultaneously to form a composite nano-matrix due to the poor solubility of NaCl/KCl and Si in the solvent. In the subsequent heat treatment, the amorphous Si is transformed into a crystalline framework composed of interconnected primary particles. The product is washed with water to remove the by-products of salts to form porous Si. Tang *et al.* designed a series of mesoporous Ge materials by the salt-templating method with NaCl and KCl as the *in situ* templates [Figure 6B]<sup>[68]</sup>. The surface area and pore size and volume can be adjusted by changing the reaction time, temperature, and calcination temperature, and the salt by-products as internal self-forming templates can be removed without an etchant. Compared to traditional template methods, this method is simpler, faster, and more environmentally friendly.

### Chemical etching method

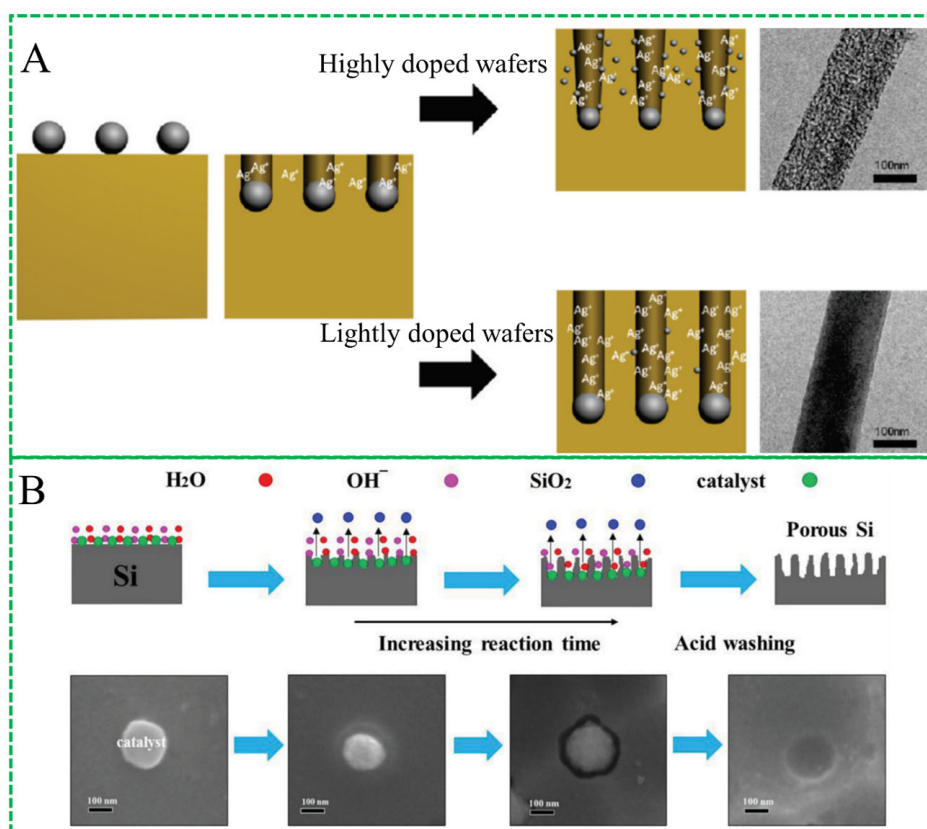
Chemical etching is an effective method to fabricate porous alloys based on different galvanic displacements or chemical activities<sup>[69]</sup>. Etching methods can be mainly divided into electrode and electroless etching. Electrode etching is controlled by the current, whereas the electroless process often involves other metal ions, such as Ag<sup>+</sup> and Cu<sup>2+</sup><sup>[70-72]</sup>. For example, porous Si nanowires have been produced with silver nitrate in HF and doped Si<sup>[73,74]</sup>. Typically, two reactions take place during etching<sup>[69]</sup>:



The porosity and pore size of porous Si can be controlled by the current density and concentration of the etchant. Zhong *et al.* studied the mechanism of the formation of porous Si nanowires in a two-step Ag-assisted electroless chemical etching method [Figure 7A]<sup>[75]</sup>. The H-terminated Si was coated with Ag by electroless deposition or physical vapor deposition and then placed into a solution containing HF and H<sub>2</sub>O<sub>2</sub> with variable concentrations for different time durations. Zhang *et al.* synthesized porous Si materials by the ferrite-assisted chemical etching of the Si substrate [Figure 7B]<sup>[76]</sup>. In this reaction, ferrite catalyzes the reaction of Si particles with glycol to produce porous Si particles. To avoid the use of the noble metal Ag, some groups have developed a less expensive Cu ion etching method. For example, porous Si has been prepared by the chemical etching of Cu nanoparticles in HF/H<sub>2</sub>O<sub>2</sub><sup>[77]</sup>. In addition to Si, porous Ge is also easy to fabricate by this method<sup>[78]</sup> using an electrolyte of HF:H<sub>2</sub>O<sub>2</sub>:H<sub>2</sub>O (2:3:1). Chemical etching can produce porous Si/Ge with different porosities, but the formation is relatively slow and involves highly corrosive HF.



**Figure 6.** (A) Schematic of synthesis route of mesoporous crystalline Si. Reproduced with permission<sup>[67]</sup> (Copyright 2014, Nature Publishing Group). (B) Synthetic route of mesoporous Ge. Reproduced with permission<sup>[68]</sup> (Copyright 2020, Elsevier Inc.).



**Figure 7.** Schematic illustrations of porous metal preparation *via* chemical etching method. (A) Schematic illustration of porous Si nanowires. Reproduced with permission<sup>[75]</sup> (Copyright 2012, American Chemical Society). (B) Schematic illustration of the formation process of porous Si wafer. Reproduced with permission<sup>[76]</sup> (Copyright 2015, Wiley-VCH Verlag).

Electrochemical etching can also produce porous alloys by applying a current<sup>[79]</sup>. The starting materials are often wafers, such as Si and Ge, and the electrolyte is typically HF. Uhlir at Bell Laboratories accidentally found that porous Si could be generated by the electrochemical etching of a Si wafer<sup>[80]</sup>. The pore formation mechanism and adjustment of the pore parameters were investigated<sup>[69]</sup>. Thakur *et al.* synthesized a



macroporous Si film by electrochemical etching in 48% HF and dimethylformamide using a constant current density of  $2 \text{ mA cm}^{-2}$ <sup>[81]</sup>. The porosity and depth of porous Si can be adjusted by the current density and HF concentration<sup>[82]</sup>. Bioud *et al.* reported the fabrication of porous Ge films by galvanostatic etching using a two-electrode system with a Ge wafer and Pt plate as the working and counter electrodes, respectively<sup>[83]</sup>. The electrolyte consisted of HF and anhydrous ethanol. Porous materials obtained by electrochemical etching have high density and purity. Although the electrochemical etching method can produce porous Si and Ge with different porosities using an applied current, it involves the use of highly corrosive HF and can cause environmental concerns<sup>[84]</sup>.

### Self-assembly methods

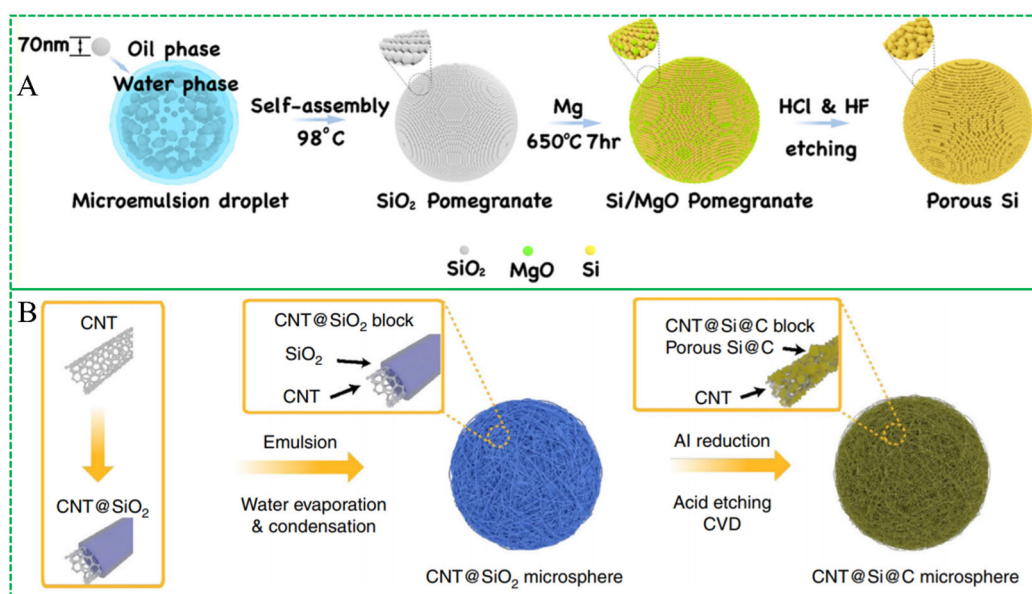
Self-assembly is attractive in the preparation of porous microstructures with nanostructures, such as nanoparticles, nanowires, and nanosheets. This method is cost-effective, scalable, simple, and can produce particles with a high tap density. Jia *et al.* designed porous microscale Si spheres composed of nanoscale crystalline Si with a uniform porous structure by self-assembly using the bottom-up microemulsion approach [Figure 8A]<sup>[85]</sup>. Jeong *et al.* adopted a cyclic iodide process to assemble microclusters comprising many kinked Si nanowires with a diameter of less than 20 nm<sup>[86]</sup>. The secondary microscale particles had considerable internal porosity, good thermodynamic stability, and high tap density. Jia *et al.* produced hierarchical porous Si microspheres of 6–8  $\mu\text{m}$  in diameter consisting of Si-coated CNTs by self-assembly [Figure 8B]<sup>[87]</sup>. By introducing molten salts, such as KCl and NaCl, a liquid environment was created to absorb heat and increase ion moving ability at a high temperature. Yao *et al.* prepared mesoporous diatomite-derived Si microspheres with NaCl as the molten liquid interface to grow Si nanocrystals by the self-assembly of mesoporous Si nanocrystals in MgR<sup>[88]</sup>. Nevertheless, there is a rate-limiting step in which the conversion of an irregular shape to a nearly spherical shape depends on the concentration of fused salts and liquid magnesium, which may dissolve each other by the interactions of ions and the negative ions in the cavity of these positive ions depend on the vibration frequency of  $\text{Mg}^{2+}$ ,  $\text{Na}^+$ , and  $\text{Cl}^-$ <sup>[89]</sup>.

## MICROSIZED POROUS ALLOYING MATERIALS FOR LIBS AND SIBS

Alloys containing Si, Ge, Sn, and Sb are promising anode materials for next-generation LIBs and SIBs because of their high theoretical capacity and volumetric capacities [Tables 1 and 2]. The porous alloy architecture comprising continuous nano-units surrounded by pores can accommodate the volume expansion and offer paths for electrolyte permeation to increase the stability of the electrodes. Moreover, porous microscale alloys have a high tap density and volumetric energy density in LIBs and SIBs. In this section, different alloys with porous structures for LIBs and SIBs are described, and the relationship between their structures and electrochemical characteristics is discussed.

### Si-based porous structures for LIBs and SIBs

Si has the unique cubic space group of  $Fd\bar{3}m$  and a large interplanar crystal spacing of 5.472 Å. It is promising anode material for LIBs on account of its high theoretical capacity, abundant resources, low cost, and non-toxicity. Si also has a low delithiation potential of  $\sim 0.4 \text{ V vs. Li}^+/\text{Li}$ , which is higher than that of graphite (below 0.2 V). In addition, Si reacts electrochemically with Li to form alloys during cycling, thus offering space to increase the Li-ion storage<sup>[90]</sup>. Chevrier *et al.* carried out first principles calculations on the Si-Li system<sup>[91]</sup>. Shenoy *et al.* derived the optimal lattice parameters of the crystalline Li-Si phases using density functional theory (DFT) calculations according to the crystal structures from the Inorganic Crystal Structure Database<sup>[92]</sup>. According to different reaction conditions, the phases in the Li-Si system were confirmed as LiSi,  $\text{Li}_2\text{Si}_7$ ,  $\text{Li}_7\text{Si}_3$ ,  $\text{Li}_{13}\text{Si}_4$ , and  $\text{Li}_{22}\text{Si}_5$ . Among them,  $\text{Li}_{22}\text{Si}_5$  showed the highest total theoretical capacity of 4,200 mAh  $\text{g}^{-1}$ <sup>[93]</sup>. By combining as many as 4.4 Li atoms, Si shows a volume expansion ( $\sim 300\%$ ) and huge stress during lithiation/delithiation, which causes pulverization, unstable SEI layers, structural collapse, and fast capacity fading. Porous microscale Si-based structures can be divided into nano-unit self-



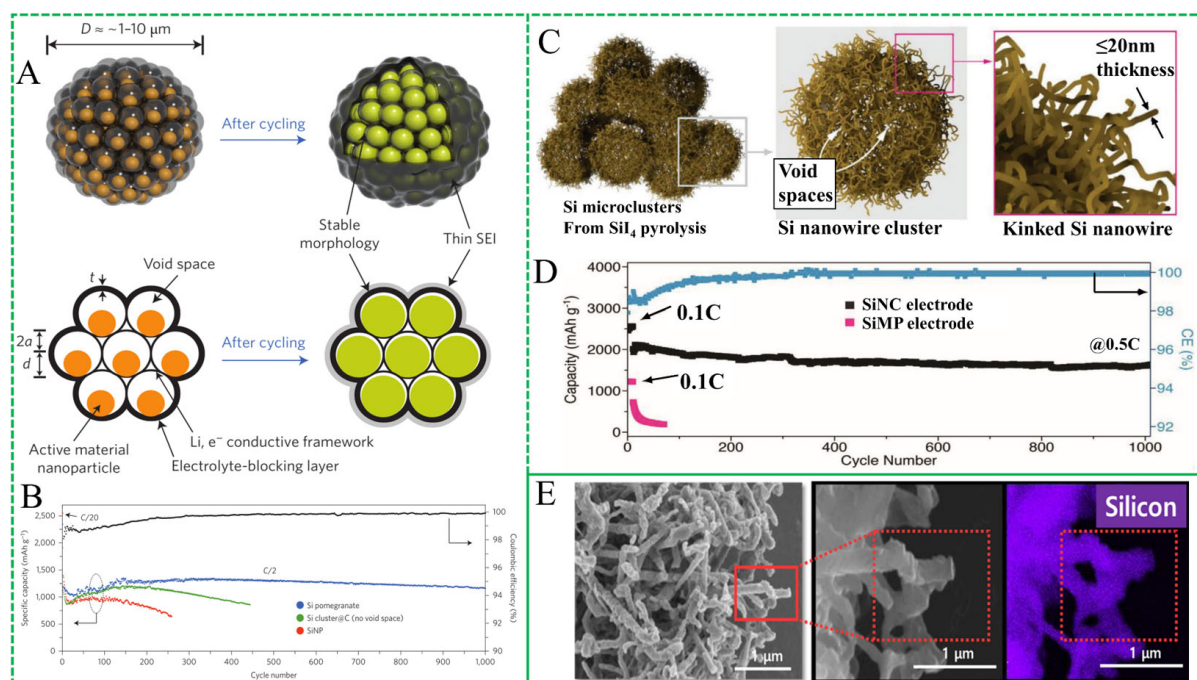
**Figure 8.** (A) Schematic illustration of preparation process of porous Si. Reproduced with permission<sup>[85]</sup> (Copyright 2018, Elsevier B.V.). (B) Schematic showing synthesis of CNT@Si@C microspheres. Reproduced with permission<sup>[87]</sup> (Copyright 2020, Nature Publishing Group).

assembled porous Si and continuous and connected skeleton porous Si, as shown in Table 3<sup>[38,46,48,72,88,94-124]</sup>.

### Nano-unit self-assembled microporous Si

Si nanomaterials with a small size and high specific surface area also exhibit high capacity and improved cycling stability but suffer from low ICE and tap density. Although it has a high gravimetric capacity of above 2,000 mAh g<sup>-1</sup>, the volumetric energy density of nano-Si is even lower than that of commercial graphite. The assembly Si nanostructures into microscale secondary particles can combine the merits of nano- and micromaterials to produce a high tap density and capacity simultaneously<sup>[125]</sup>. Moreover, the nano-units self-assembled in microscale porous Si have many pores to accommodate volume expansion and reduce the volume change on the particle level in LIBs<sup>[112]</sup>. Porous Si consists of nano-units for lithiation from end-to-end, whereas solid larger Si particles are surface-to-center<sup>[126]</sup>.

Liu *et al.* fabricated yolk-shell spherical Si pomegranate microbeads with a diameter of up to 10 μm *via* the self-assembly of Si@SiO<sub>2</sub> nanoparticles with the aid of emulsifiers [Figure 9A]<sup>[127]</sup>. The spherical Si pomegranate microbeads show a high reversible capacity of 2,350 mAh g<sup>-1</sup> at a rate of C/20 (1 C = 4,200 mA g<sup>-1</sup>) in conjunction with a capacity retention of 97% after 1,000 cycles at C/2, significantly better than that of Si NPs [Figure 9B]. The enhanced performance of these composites stems from the incorporation of carbon and the smaller particle sizes, with the well-defined internal space allowing Si to expand without changing the secondary particle size. Jia *et al.* reported porous Si (p-Si) comprised of Si nanoparticles<sup>[85]</sup>. The unique porous structure endows the materials with good electrical contact and provides a fast route for the transportation of lithium ions, as well as good internal stress accommodation. As a result, p-Si exhibits a reversible capacity of 2,500 mAh g<sup>-1</sup> at 0.26 A g<sup>-1</sup> with an ICE of 75% and a cycling stability capacity of 1,467 mAh g<sup>-1</sup> at 2.6 A g<sup>-1</sup> after 370 cycles with a capacity retention of 83%. Furthermore, Shi *et al.* designed a porous microscale structure made of TiO<sub>2</sub>-coated Si nanoparticles in building blocks that were further filled with hierarchical Si@TiO<sub>2</sub>@C (SA-SiTC)<sup>[128]</sup>. In this composite, the carbon filler and TiO<sub>2</sub> layer act as a mechanical buffer and electrolyte reservoir, respectively. The SA-SiTC electrode displayed long cycling stability (842.6 mAh g<sup>-1</sup> after 1,000 cycles at 2 A g<sup>-1</sup>), high volumetric capacity (174 mA h cm<sup>-3</sup>) and ICE



**Figure 9.** (A) Structural evolution of pomegranate Si microparticles before and after electrochemical cycling. (B) Cycling performance of the Si pomegranate and other structures at C/2. Reproduced with permission<sup>[127]</sup> (Copyright 2014, Springer Nature). (C) Microscale Si particles incorporating self-kinked Si nanowire clusters. (D) Cycling performance of samples at 0.5 C. Reproduced with permission<sup>[86]</sup> (Copyright 2020, Wiley-VCH Verlag). (E) SEM images of Si nanowires and mapping of Si. Reproduced with permission<sup>[129]</sup> (Copyright 2020, Elsevier B.V.).

(80.9%), and a stable SEI layer.

In addition to Si nanoparticles, Si nanowires can be assembled into porous secondary microscale particles. Jia *et al.* applied self-assembly to prepare hierarchical porous Si microspheres of 6–8  $\mu\text{m}$  in diameter with Si-coated CNTs (CNT@Si@C)<sup>[87]</sup>. The CNT@Si@C electrode with a practical mass loading ( $3 \text{ mAh cm}^{-2}$ ) showed a specific capacity of  $750 \text{ mAh g}^{-1}$ , an initial swelling of  $< 20\%$  at 100% state-of-charge and a capacity retention of 92% over 500 cycles. Owing to the unique highly porous yarn-ball-like structure with high porosity and good mechanical strength, the CNT@Si@C microspheres showed the expected effect of suppressed swelling of porous Si particles upon lithiation to maintain the overall structural integrity. Jeong *et al.* fabricated Si clusters with an average size of  $2.7 \mu\text{m}$  by a silicon iodide ( $\text{SiI}_4$ ) decomposition method, as shown in Figure 9C<sup>[86]</sup>. The porous Si was composed of kinked nanowires with diameters of less than 20 nm. The kinked Si nanowires not only formed voids but also contacted each other to yield electrolyte transfer channels for better ionic conductivity and interconnections for better electronic conductivity. The nanowire-assembled porous particles have ample voids between the nanowires and can accommodate large volume changes. As a result, they showed a capacity of  $2,784.7 \text{ mAh g}^{-1}$  at 0.1 C with an ICE of 82.4%, together with a superior capacity retention of 83.6% for 1,000 cycles [Figure 9D]. Recently, Choi *et al.* produced porous microscale Si consisting of nanowires with a diameter of 300 nm and a length of  $> 1 \mu\text{m}$  by self-assembly using a molten salt electrochemical reduction method from RH-derived  $\text{SiO}_2$ <sup>[129]</sup>. As shown in Figure 9E, the product has a spherical shape with a porous structure. The porous Si anode has a high capacity of  $3,161 \text{ mAh g}^{-1}$  at 0.05 C, corresponding to an ICE of 84% and a capacity of  $2,550 \text{ mAh g}^{-1}$  after 100 cycles at 0.2 C. Even at a high rate of 1 C, the capacity is maintained at  $1,371 \text{ mAh g}^{-1}$ .

### Continuous microporous Si

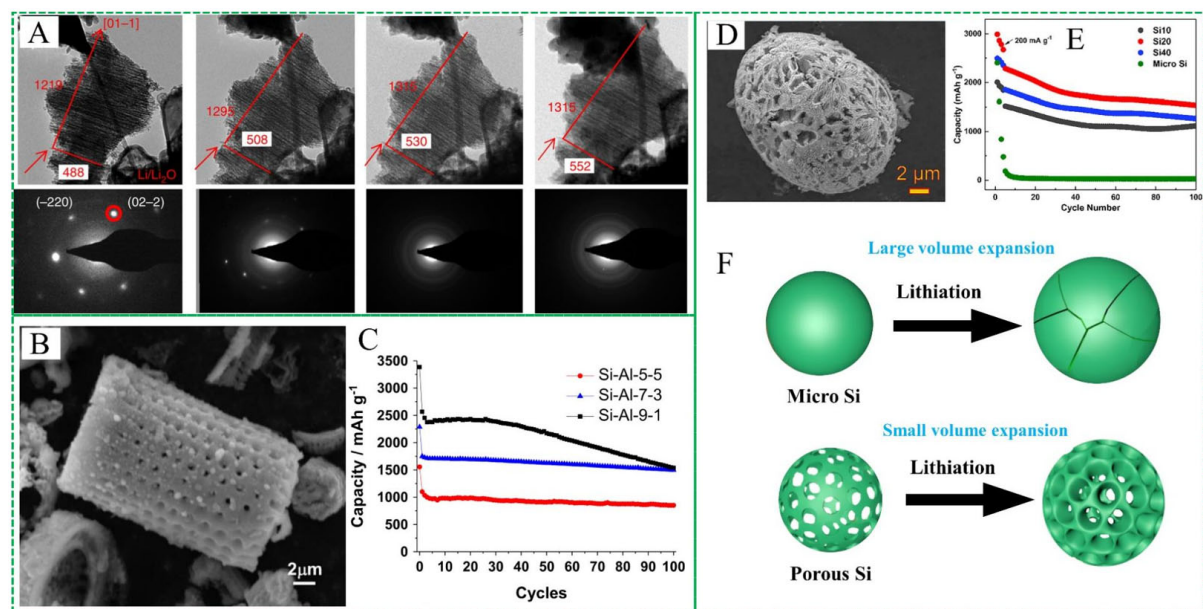
Different from porous particles made of nano-units, 3D continuous porous Si networks containing continuous nano-skeletons may have better structural stability to alleviate fracture during volume changes. Continuous nanoporous Si microparticles have been demonstrated to improve the cycling characteristics because the connected 3D ligaments disperse the stress during the lithiation/delithiation or sodiation/desodiation of Si. Kim *et al.* reported 3D porous bulk Si microparticles fabricated by thermal annealing and etching of the composites of butyl-capped Si gels and SiO<sub>2</sub> nanoparticles<sup>[130]</sup>. Because the thin pore wall of ~40 nm can accommodate a large strain without pulverization, the porous Si particles maintain a high charging capacity of 2,800 mAh g<sup>-1</sup> at a current density of 2,000 mA g<sup>-1</sup> after 100 cycles, together with excellent rate performance. Jia *et al.* designed lotus-root-like 3D mesoporous Si by MgR and acid etching<sup>[98]</sup>. Porous Si has uniform mesopores and the particles are composed of 30 nm Si crystallites that facilitate fast electrode kinetics. The 3D mesoporous Si has high electrochemical reversibility with a capacity retention of 94.4% at 100 cycles.

Liu and co-workers reported a sub-micrometer mesoporous Si sponge prepared by anodization, and the porous Si showed a capacity of 750 mAh g<sup>-1</sup> based on the total electrode weight with an 80% capacity retention over 1,000 cycles<sup>[102]</sup>. *In situ* TEM demonstrated that the mesoporous Si sponge limits the volume expansion of the active particles and prevents pulverization of the bulk Si particles [Figure 10A]. Choi *et al.* fabricated porous Si microparticles via an aluminothermic reaction and subsequent MgR [Figure 10B]<sup>[105]</sup>. Because of the special porous structure, which can accommodate large volume changes and facilitate ion transportation during cycling, the porous Si/Al<sub>2</sub>O<sub>3</sub> microcomposite exhibited outstanding stability with a capacity of 1,500 mAh g<sup>-1</sup> after 100 cycles at C/5 and a small volume expansion of 34% [Figure 10C]. Tao *et al.* adopted chemical dealloying to prepare a series of porous Si materials by etching Al-Si alloys [Figure 10D]<sup>[131]</sup>. The porous Si maintained a spherical structure and the pores were uniformly distributed. As a result, the porous Si had a high capacity of 3,004 mAh g<sup>-1</sup> at 500 mA g<sup>-1</sup> in the first cycle with an ICE of 81% [Figure 10E]. The reversible capacity of porous Si was maintained at 1,525 mAh g<sup>-1</sup> after 100 cycles at 1,000 mA g<sup>-1</sup>. This remarkable stability was attributed to the porous structure, which alleviates the volume change during repetitive lithiation/delithiation [Figure 10F].

Mu *et al.* investigated the impact of commercial Si nanoparticles (C-SiNP) and mesoporous Si microparticles (MP-Si)<sup>[95]</sup>. The MP-Si showed outstanding cycling stability and a high reversible capacity of 1,793 mAh g<sup>-1</sup> after 120 cycles at 200 mA g<sup>-1</sup>. The Li-ion storage properties benefit from the two-dimensional (2D) nanoplates and abundant mesopores in the Si microparticles, which not only promote immersion of the electrolyte and the transportation of lithium ions, but also buffer the volume expansion and ensure the structural stability of the electrode. Sohn and co-workers prepared 3D porous Si microparticles by alkali and acid etching<sup>[38]</sup>. The 3D porous Si electrode showed a high initial charge capacity of 2,919 mAh g<sup>-1</sup> with an ICE of 76.5% and a capacity of 1,222 mAh g<sup>-1</sup> after 200 cycles with an average CE of ~99%. The excellent electrochemical properties of the 3D porous Si suggest that the etching-induced morphological modification, including pore enlargement and reduction of the Si size, is highly effective in improving the cycling characteristics.

Porous ant-nest-like microscale Si (AMPSi) has been produced by a low-cost and scalable top-down approach, involving thermal nitridation of a Mg-Si alloy and removal of the Mg<sub>3</sub>N<sub>2</sub> by-product in an acidic solution [Figure 11A and B]<sup>[51]</sup>. The high porosity of AMPSi allows the inward expansion of the 3D interconnected Si nano-ligaments during cycling, which gives rise to high structural stability and negligible particle-level outward expansion [Figure 11C]. Therefore, after carbon deposition, the AMPSi and C composites (AMPSi@C) showed a high ICE of 80.3%, reversible capacities of 2,134 and 1,271 mAh g<sup>-1</sup> at 0.1 and 0.5 C (1 C = 4,200 mA g<sup>-1</sup>), respectively, and a 90% capacity retention from 20 to 1,000 cycles in a





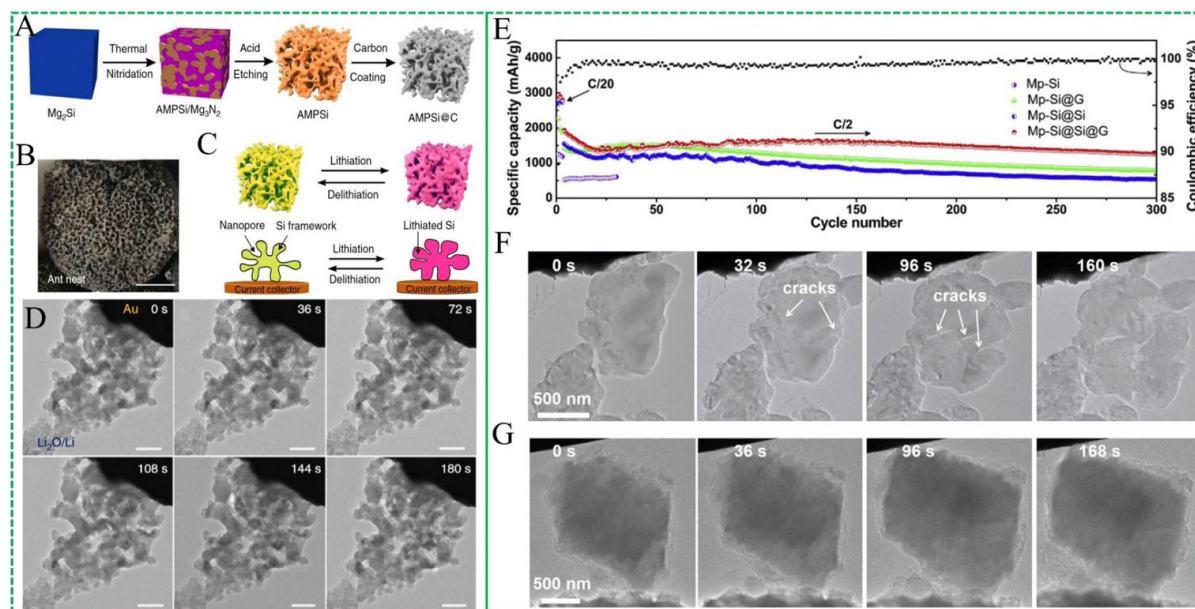
**Figure 10.** (A) TEM images and selected area electron diffraction patterns of mesoporous Si sponge particles at different lithiation states. Reproduced with permission<sup>[102]</sup> (Copyright 2014, Nature Publishing Group). (B) SEM images of macroporous Si structure. (C) Cycling performance of porous Si/Al<sub>2</sub>O<sub>3</sub> composite at C/5. Reproduced with permission<sup>[105]</sup> (Copyright 2015, Elsevier B.V.). (D) SEM images of porous Si. (E) Cycling performance of different porous Si samples at 500 mA g<sup>-1</sup>. (F) Volume changes can be restricted by porous construction during cycling. Reproduced with permission<sup>[131]</sup> (Copyright 2019, Elsevier Inc.).

lithium-ion half-cell. The AMPSi@C//NCM full cell exhibited a high reversible capacity of 134 mAh g<sup>-1</sup> at 0.5 C (1 C = 160 mA g<sup>-1</sup>) with a capacity retention of 84% for over 400 cycles together with a high energy density of 502 Wh kg<sup>-1</sup>. *In situ* TEM indicated that AMPSi@C remained stable during lithiation and delithiation, with volumetric expansion introduced to the pores to restrict outward expansion [Figure 11D].

Wang *et al.* designed mesoporous Si microparticles by the thermal disproportionation of low-cost SiO microparticles and subsequent removal of the SiO<sub>2</sub> by-product<sup>[132]</sup>. After graphene cage-encapsulated Si skin-sealed mesoporous Si (Mp-Si@Si@G) microparticles were obtained by a surface-engineering strategy by depositing a dense silicon skin onto each mesoporous Si (Mp-Si@Si) microparticle, encapsulation was performed to form a conformal graphene cage. Mp-Si@Si@G showed a high reversible specific capacity of 1,246 mAh g<sup>-1</sup> after 300 cycles at a rate of C/2, which can be ascribed to the optimal specific surface area and suitable porosity of Mp-Si@Si@G, consequently decreasing the electrolyte accessible area, SEI formation and irreversible Li consumption [Figure 11E]. The morphology of Mp-Si@Si@G was monitored by *in situ* TEM during lithiation and an apparent volume expansion of the dense Si microparticles was observed [Figure 11F]. Cracks appeared after only 32 s and widened with time. At 160 s, the dense Si microparticles fractured abruptly into smaller particles. In contrast, the structures of the Mp-Si@Si@G microparticles were well maintained throughout the whole lithiation process [Figure 11G] and remained intact even after full lithiation because of the sufficient inner pore space and the mechanically strong graphene cage that limited volume expansion.

Si-based alloys have been developed as anode materials for SIBs with a capacity of 954 mAh g<sup>-1</sup><sup>[133]</sup>, and the volume change of NaSi formed from Si is ~244%, which is much smaller than that for Ge-, Sn- and Sb-based anodes in SIBs. In general, the sodiation of Si has different phase behaviors, insertion voltages, and kinetic barriers compared to the reaction with Li. For instance, because of the difference in the ionic radii of Na<sup>+</sup>



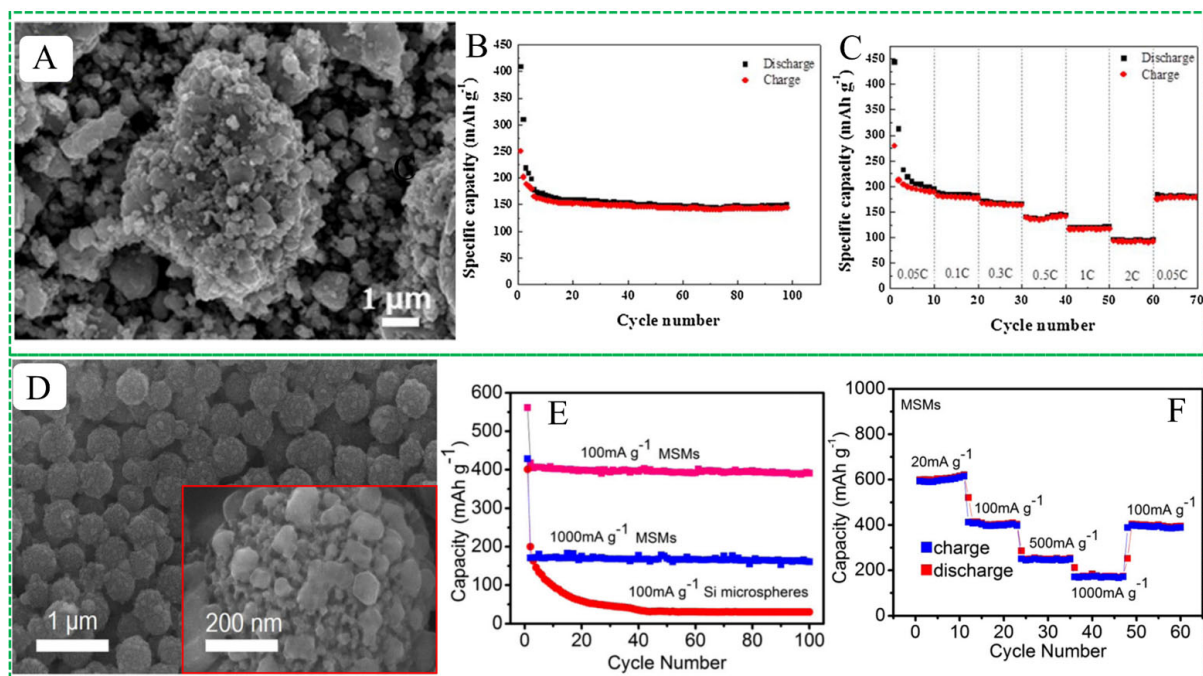


**Figure 11.** (A) Schematic showing preparation of AMPSi and AMPSi@C. (B) Photograph of an ant nest (scale bar = 20 cm). (C) Schematic of lithiation/delithiation process of ant-nest-like microscale porous Si particles. (D) Time-resolved TEM images depicting the lithiation process of AMPSi@C electrode (scale bar = 200 nm). Reproduced with permission<sup>[51]</sup> (Copyright 2019, Nature Publishing Group). (E) Cycling performance of Mp-Si with different surface-engineering treatments. Time-lapse TEM images of lithiation of (F) dense Si and (G) Mp-Si@Si@G microparticles. Reproduced with permission<sup>[132]</sup> (Copyright 2019, Elsevier B.V.).

(0.97 Å) and Li<sup>+</sup> (0.68 Å), the insertion of Na into crystalline Si is limited<sup>[134,135]</sup>. Xu *et al.* obtained amorphous Si particles by thermal plasma CVD of silane, which showed reversible Na-ion storage with a capacity of 270 mAh g<sup>-1</sup> at 20 mA g<sup>-1</sup><sup>[134]</sup>. Wu and co-workers demonstrated the fabrication of amorphous Si-rich interior cores surrounded by a Sn shell (a-Si<sub>SN</sub>) via mechanical alloying<sup>[136]</sup>. The amorphous sponge-like a-Si<sub>SN</sub> has pores [Figure 12A], leading to a reversible capacity of 151 mAh g<sup>-1</sup> after 100 cycles at 36.25 mA g<sup>-1</sup> and a high rate capacity of 143 mAh g<sup>-1</sup> at 725 mA g<sup>-1</sup> [Figure 12B and C]. Recently, Qiu *et al.* prepared mesoporous Si microspheres (MSMs) with homogeneously distributed mesopores ranging from 1 to 10 nm *via* the MgR of SiO<sub>2</sub><sup>[137]</sup>. As shown in Figure 12D, the mesoporous Si microspheres with abundant mesopores exhibited a high reversible capacity of 390 mAh g<sup>-1</sup> at 100 mA g<sup>-1</sup> after 100 cycles [Figure 12E] and a high rate capacity of 160 mAh g<sup>-1</sup> at a high current density of 1,000 mA g<sup>-1</sup> [Figure 12F]. The good cycling and excellent rate capability can be attributed to the small particle size and mesoporous structure. However, for the practical application of Si materials in SIBs, several issues still need to be addressed, including structural optimization, electrolyte design, and the development of novel binders<sup>[138-140]</sup>.

### Ge-based porous structures for LIBs and SIBs

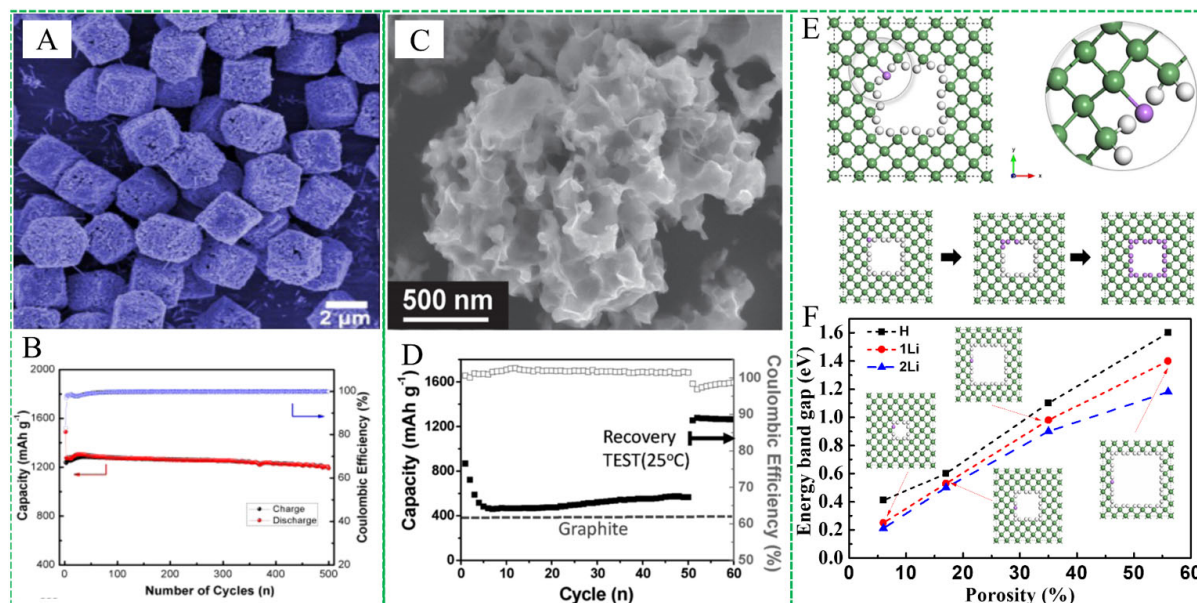
Ge is in the same chemical group as Si and is regarded as a promising alloying anode material because of its high theoretical capacities [Tables 1 and 2] and suitable operating voltages for LIBs and SIBs. Moreover, the conductivity of Ge is 100 times higher than that of Si. Similarly, Ge anodes also suffer from severe volume expansions, leading to pulverization during lithiation/delithiation. Porous Ge has garnered significant attention since the pores in porous Ge can act as volume expansion buffers to improve the cycling stability. Table 4<sup>[39,63,141-149]</sup> lists the synthesis strategies and compares the electrochemical properties of different porous Ge anode materials for LIBs.



**Figure 12.** (A) SEM of a-Si<sub>3</sub>N<sub>4</sub>. (B) Long-term cycling properties of a-Si<sub>3</sub>N<sub>4</sub> electrode. (C) Rate performance of a-Si<sub>3</sub>N<sub>4</sub>. Reproduced with permission<sup>[136]</sup> (Copyright 2016, Elsevier Ltd.). (D) SEM images of MSMs. (E) Discharge capacity retention of MSMs and Si microspheres. (F) Rate performance of MSMs. Reproduced with permission<sup>[137]</sup> (Copyright 2018, Springer Verlag).

Yang and co-workers prepared mesoporous Ge microparticles by a mechanochemical reaction of GeO<sub>2</sub> and Mg powders and subsequent etching in HCl<sup>[142]</sup>. The mesoporous Ge showed a reversible capacity of 950 mAh g<sup>-1</sup> and a capacity of 789 mAh g<sup>-1</sup> after 20 cycles at a current density of 150 mA g<sup>-1</sup>. Jia *et al.* prepared 3D macroporous Ge (p-Ge) microparticles with a hexagonal-like morphology by MgR and HCl etching<sup>[63]</sup>. The p-Ge anode had a high reversible capacity of 1,131 mAh g<sup>-1</sup> at 1 C after 200 cycles and a high rate capability with a capacity of 717 mAh g<sup>-1</sup> at 5 C (1 C = 1,624 mA g<sup>-1</sup>). The internal space in 3D p-Ge buffers the volume change of Ge during cycling and preserves the structural stability of the anode materials. Cui and his team synthesized Ge microcubes with a hierarchical porous structure directly on a titanium foil by a simple hydrogen reduction method [Figure 13A]<sup>[148]</sup>. The Ge microcubes showed good cycling and rate characteristics due to the voids, such as a high ICE of 91.8% stemming from the high crystallinity of Ge in reversible lithium insertion and extraction, a less adverse side reaction for irreversible Li loss, and unique hierarchical porous structure for easier electrolyte penetration. The Ge microcubes exhibited a high retention capacity of 1,204 mAh g<sup>-1</sup> after 500 cycles at a rate of 1 C, corresponding to a capacity retention of 94.1% from the first cycle, and a good rate of 1,121 mAh g<sup>-1</sup> at a high rate of 50 C [Figure 13B].

Choi and co-workers synthesized porous Ge by metallothermic reduction using two different metal reductants by the zincthermic reduction reaction (ZnRR) and MgR, respectively<sup>[150]</sup>. Figure 13C shows the SEM image of the ZnRR-synthesized Ge particles [Ge (ZnRR)], which have a mesoporous structure with numerous mesopores. With mesopores in the inner parts, the porous Ge provides extra spaces for the expansion of particles and accommodates the large volume change during lithiation/delithiation. The Ge (ZnRR) electrode showed a high ICE of ~85%, excellent cycling stability at a low temperature of -20 °C, and a high specific capacity of 566 mAh g<sup>-1</sup> at a rate of 0.5 C after 50 cycles [Figure 13D]. The Ge//LiFePO<sub>4</sub> full cell exhibited an ICE value of 98% in the first cycle and retention of 80% at 0.5 C after 50 cycles at -20 °C. Mishra *et al.* synthesized porous microscale Ge by the hydrogen reduction of GeO<sub>2</sub><sup>[151]</sup>. The porous Ge

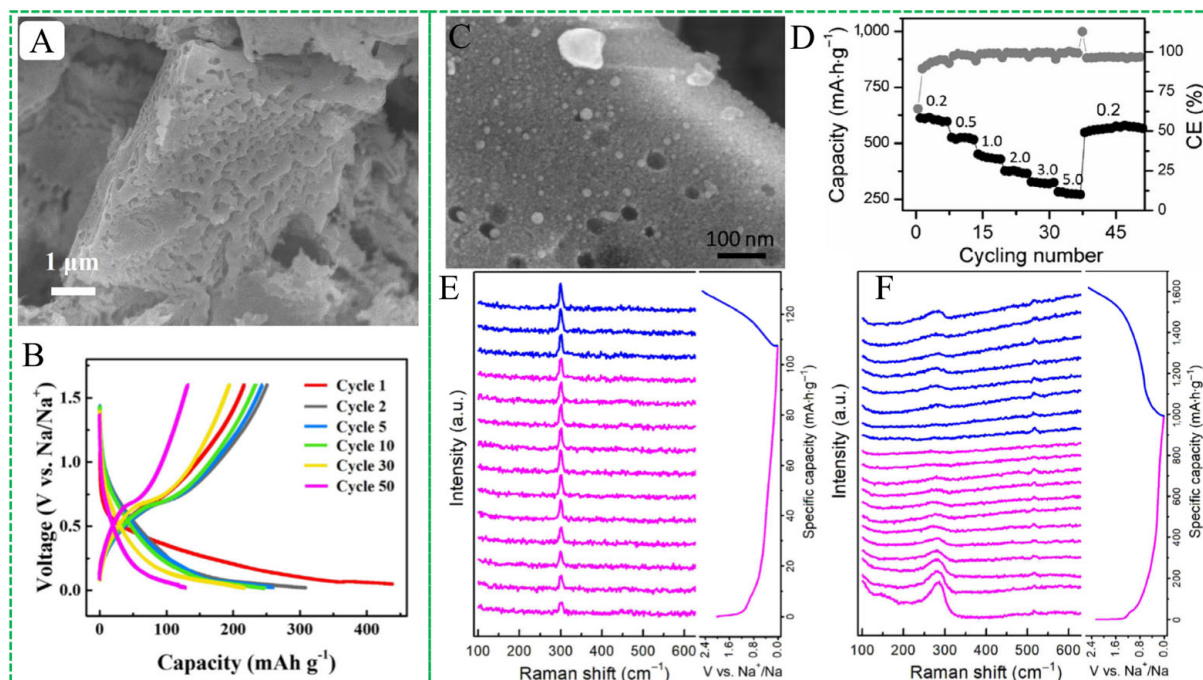


**Figure 13.** (A) SEM images of porous Ge microcubes. (B) Cycling performance of porous Ge microcubes. Reproduced with permission<sup>[148]</sup> (Copyright 2015, American Chemical Society). (C) SEM of mesoporous Ge. (D) Cycling performance of Ge (ZnRR) electrodes. Reproduced with permission<sup>[150]</sup> (Copyright 2017, Wiley-VCH Verlag GmbH & Co.). (E) Top view of pGe with 18.05% porosity and one surface Li. In the lower panel, the process of the gradual lithiation is shown with one, four, and twenty Li surface atoms in sequence. Green, white and purple balls represent Ge, H, and Li atoms, respectively. (F) Band gap evolution as a function of the porosity of fully H passivated pGe (dark squares) and pGe with one (red circles) and two (blue triangles) Li atoms. Reproduced with permission<sup>[152]</sup> (Copyright 2020, John Wiley & Sons Inc.).

electrode showed a reversible capacity of  $1,300 \text{ mAh g}^{-1}$  after 340 cycles at  $1,000 \text{ mA g}^{-1}$  and a high capacity of  $437 \text{ mAh g}^{-1}$  at  $16 \text{ A g}^{-1}$ . The excellent long-term cycling can be attributed to the porous morphology of the Ge electrode, which can maintain the stress induced by Li ions without crushing, provide good electrolyte infiltration and shorten the Li-ion diffusion length. Sosa *et al.* studied the effects of surface and interstitial Li on the electronic properties of porous Ge (pGe) using DFT calculations and showed that diffusion is easier due to the ion conductivity [Figure 13E and F]<sup>[152]</sup>. The porous framework of Ge not only facilitates the fast diffusion of ions and electrons but also buffers the volume change during cycling.

Kohandehghan *et al.* reported that amorphous Ge can reduce the nucleation barrier of the  $\text{Na}_x\text{Ge}$  phase and improve solid-state ion diffusion to enhance Na-ion storage<sup>[153]</sup>. Lu *et al.* also demonstrated that Ge can be readily and reversibly sodiated after turning crystalline Ge nanowires into amorphous ones in the initial lithiation step<sup>[154]</sup>. The amorphous Ge nanowires exhibited a 300% volumetric expansion upon sodiation, corresponding to the formation of  $\text{Na}_{1.6}\text{Ge}$ . Li *et al.* prepared porous Ge microparticles with a Mn-Ge alloy by selective corrosion<sup>[155]</sup>. The porous Ge microparticles showed a broad ligament size distribution in the range between 100 and 300 nm, as shown in Figure 14A. The porous Ge microparticle electrode showed a reversible capacity of  $260 \text{ mAh g}^{-1}$  in the initial cycle and good cycling stability over 50 cycles at C/5 [Figure 14B]. Yi *et al.* synthesized mesoporous amorphous Ge microparticles by acid etching the Zintl-phase  $\text{Mg}_2\text{Ge}$  at room temperature and studied the Na-ion storage mechanism in meso-porous amorphous Ge (A-Ge) by *in situ* Raman scattering and *ex situ* XRD<sup>[156]</sup>. As shown in Figure 14C, A-Ge with a rough surface showed a high reversible charge capacity of  $600 \text{ mAh g}^{-1}$ , a capacity retention of 90.2% after 50 cycles at 0.2 C, and a rate capacity of  $273 \text{ mAh g}^{-1}$  at 5 C [Figure 14D]. The *in situ* Raman spectrum in Figure 14E obtained during sodiation/desodiation reveals no distinct peak shift or peak intensity change in C-Ge during the first charging/discharging cycle. This is because Na ions cannot be easily inserted into the





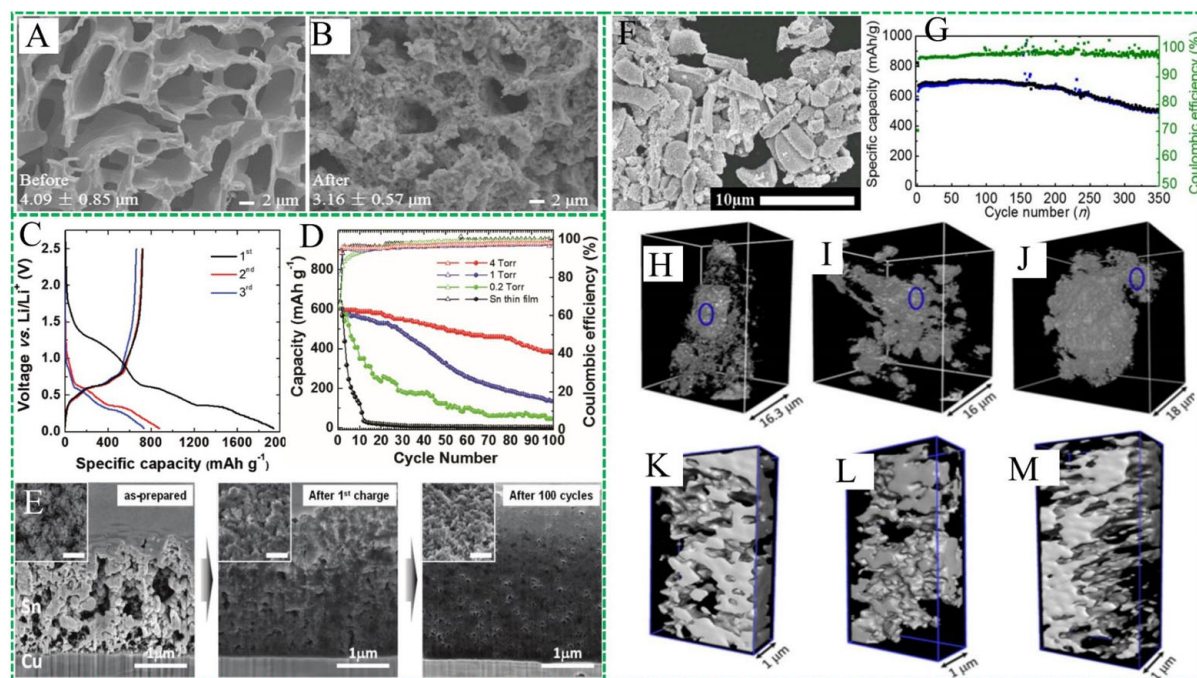
**Figure 14.** (A) SEM images of porous Ge microparticles. (B) Galvanostatic charge-discharge curves of porous Ge microparticles. Reproduced with permission<sup>[155]</sup> (Copyright 2019, Elsevier). (C) SEM image of mesoporous A-Ge microparticles. (D) Rate capability from 0.2 to 5 C of A-Ge. *In-situ* Raman spectrum of (E) crystalline and (F) amorphous Ge during the first discharge/charge curve. Reproduced with permission<sup>[156]</sup> (Copyright 2019, Tsinghua University Press).

interior of C-Ge during discharging. However, the mesoporous A-Ge showed an apparent signal change during charging/discharging. As shown in [Figure 14F](#), the *in situ* Raman spectrum discloses that the mesoporous amorphous Ge is active with Na in the SIB. The amorphous phase of the Ge anode lowers the sodiation barrier and increases the Na<sup>+</sup> storage. The mesoporous architecture also provides fast electronic/ionic transportation channels to enhance the rate and provides space for the volume expansion.

### Sn-based porous structures for LIBs and SIBs

Like Si and Ge, metallic Sn can alloy with Li and Na as an alternative to traditional graphite anodes due to its high theoretical capacity [[Tables 1](#) and [2](#)], high electrical conductivity, moderate operating voltage, and safety. However, the practical application of metallic Sn to LIBs and SIBs is affected by the huge volume change, aggregation of Sn particles during cycling, serious pulverization, and loss of electrical connection with the current collector. The newly formed surface consumes Li by forming the SEI film, and the aggregation of particles leads to poor kinetics, fast capacity decay, and poor cyclability. Direct or indirect methods to alleviate the volume expansion by reducing the particle size and introducing an accommodation space or buffer are currently being studied.

Pore formation can improve the electrochemical properties of electrode materials. However, porous Sn obtained by a simple method still presents significant challenges due to the low melting point and inevitable electrochemical agglomeration of Sn. Song *et al.* fabricated porous 3D continuous microscale Sn from immiscible Al-Sn alloys<sup>[157]</sup>. The microporous Sn anode showed an outstanding initial capacity of 818 mAh g<sup>-1</sup> and a high CE of 99%. The porous structure of Sn still retained the porous framework after first cycling [[Figure 15A](#) and [B](#)]. Ryu *et al.* prepared porous Sn consisting of homogeneous Sn particles prepared by vacuum deposition<sup>[158]</sup>. The porosity of the Sn exceeded 98% and the porous Sn anode showed a high initial discharge capacity of 1,939 mAh g<sup>-1</sup> and a charge capacity of 714 mAh g<sup>-1</sup> at 0.1 C [[Figure 15C](#)]. The

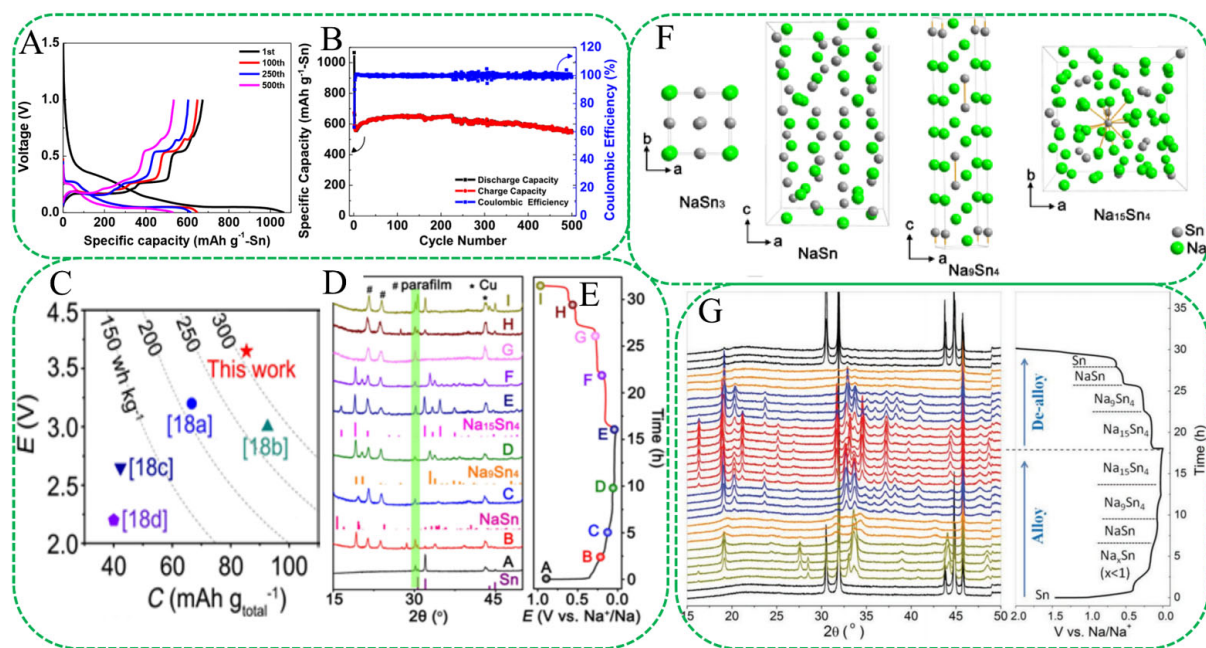


**Figure 15.** SEM images of porous Sn structure (A) before and (B) after lithiation/delithiation process for first cycling. Reproduced with permission<sup>[157]</sup> (Copyright 2015, Springer). (C) Charge/discharge profiles of porous Sn anode during the first three cycles. (D) Cycling performance of Sn samples. (E) Cross-sectional SEM images of the as-prepared sample and after 100 cycles of porous Sn anode. Reproduced with permission<sup>[158]</sup> (Copyright 2019, John Wiley & Sons Ltd.). (F) SEM images of porous Sn. (G) Cycling performance of porous Sn. (H) Pristine sample. (I) Electrode recovered after one electrochemical cycle at 1.2 V. (j) Fully lithiated sample at 70 mV. (H), (I) and (J) show the magnified subsurface renderings of the highlighted areas in panels (K), (L), and (M), respectively. Reproduced with permission<sup>[159]</sup> (Copyright 2016, American Chemical Society).

reversible capacity of the porous Sn anode changes from 603 to 378 mAh g<sup>-1</sup> at a rate of 1 C after 100 cycles, corresponding to a capacity retention of 63% [Figure 15D]. As shown in Figure 15E, the volume expansion of the porous Sn anode was only 34% during the first lithiation. Cook *et al.* prepared porous tin (P-Sn) particles by MgR [Figure 15F]<sup>[159]</sup>. The P-Sn particles exhibited a high capacity of 578 mAh g<sup>-1</sup> and the maximum capacity remained at 80% after 300 cycles at 250 mA g<sup>-1</sup> [Figure 15G]. The good cycling performance of NP-Sn was attributed to the porous structure that buffers the volume change during alloying. X-ray microscopy showed that the porosity is retained in both the charged and discharged states. As shown in Figure 15H-J, the size distribution of the P-Sn particles was wide (1-20 μm). The pristine particles showed an interconnected network of random mesopores [Figure 15K] arising from dealloying. Figure 15L and M show that the initial random pores and interconnected ligaments still exist even in a fully lithiated state with volume expansion (~300%). Therefore, the porous structure not only accommodates Li ions during volume expansion but also retains space for electrolyte diffusion.

Metallic Sn with a porous structure is also promising in SIBs. Wang *et al.* studied the two-step reaction for sodiation of Sn by *in situ* TEM, which revealed a two-phase reaction mechanism with a modest volumetric expansion of ~60% and a single-phase reaction with a large volume expansion of ~420% after full sodiation<sup>[160]</sup>. The large volume expansion/contraction exerted strong mechanical pressure on the Sn nanoparticles, resulting in the production of cracks, serious pulverization of Sn, continuous growth of the SEI, slow kinetics of Na ions, low CE, and rapid electrode failure due to the loss of contact between particles. The porous structure not only provided more space for the volume expansion of Sn but also reduced the ion transfer distance to improve the kinetics. Kim *et al.* prepared porous Sn (PSn) by the phase-inversion

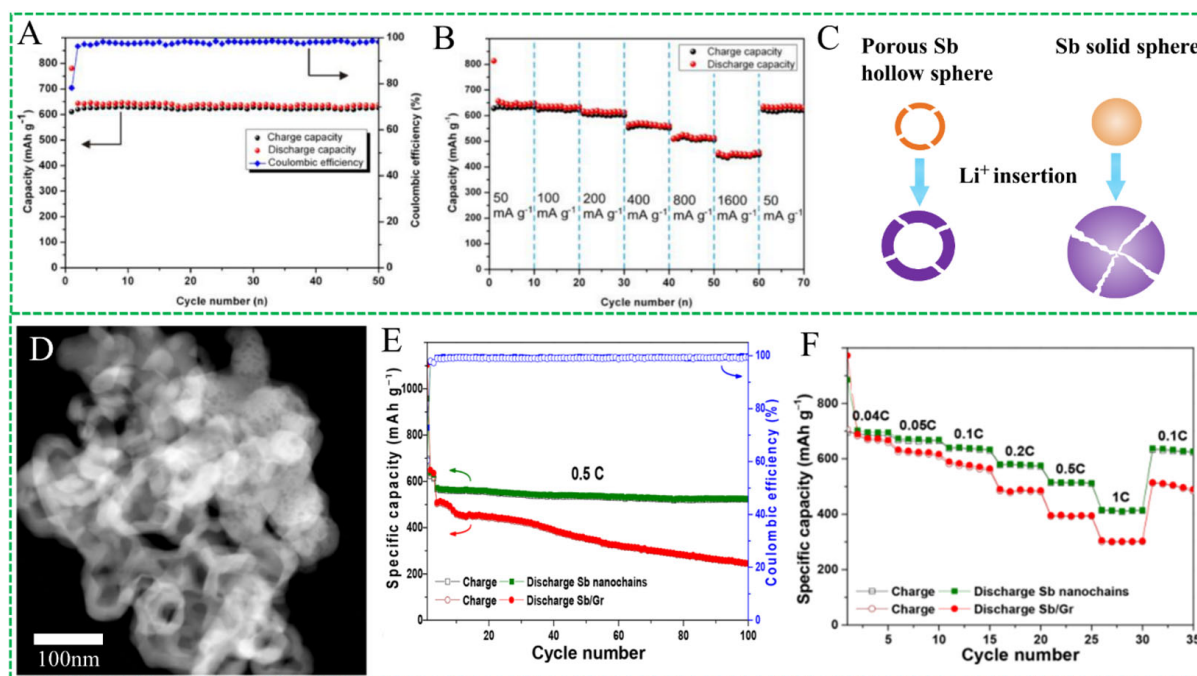




**Figure 16.** (A) Charge-discharge profiles of PSn for 500 cycles. (B) Cycling performance of PSn. Reproduced with permission<sup>[161]</sup> (Copyright 2016, Elsevier). (C) Comparison of voltage and specific capacity of a full battery. (D) XRD patterns of porous Sn/Cu anode at different states during the first cycle. (E) Voltage vs. specific capacity plot for different states. (F) Refined crystal structures of intermediates, NaSn<sub>3</sub>, NaSn, Na<sub>9</sub>Sn<sub>4</sub>, and Na<sub>15</sub>Sn<sub>4</sub>, in discharging process. Reproduced with permission<sup>[162]</sup> (Copyright 2018, Wiley-VCH Verlag GmbH & Co.). (G) *In situ* XRD patterns of micro-sized Sn during the first cycle. Reproduced with permission<sup>[164]</sup> (Copyright 2016, Wiley-Blackwell).

technique for anode materials in SIBs<sup>[161]</sup>. The PSn electrode showed a high initial capacity of 1,066 mAh g<sup>-1</sup> and a reversible capacity of 519 mAh g<sup>-1</sup> after 500 cycles at 0.5 C [Figure 16A and B].

Wang *et al.* obtained 3D porous Sn by tuning the redox potential of Cu<sup>+</sup>/Cu with a ligand of thiourea to trigger the replacement reaction between Cu and Sn<sup>2+</sup><sup>[162]</sup>. The porous Sn electrode showed a high reversible capacity of 700 mAh g<sup>-1</sup> at 2,500 mA g<sup>-1</sup> for 400 cycles, which was significantly better than that of the bare Sn. The full battery of Sn/Cu//Na<sub>3</sub>(VO<sub>0.5</sub>)<sub>2</sub>(PO<sub>4</sub>)<sub>3</sub>F<sub>2</sub> had high energy and power densities of 311.7 Wh kg<sup>-1</sup> and 182.5 W kg<sup>-1</sup>, respectively [Figure 16C], and good cycling performance for 200 cycles without any obvious degradation observed. As shown in Figure 16D and E, the electrochemical reaction was studied by XRD in selected discharging and charging states. During discharging, the new diffraction peak belonging to the cubic phase of NaSn<sub>3</sub> was found in state B (discharging to 0.2 V). After discharging to 0.1 V (state C), tetragonal NaSn with a space group of *I41/acd* could be observed. Upon discharging to 0.06 V (state D), the characteristic diffraction peaks of Na<sub>9</sub>Sn<sub>4</sub> became evident and after full discharging to 0.01 V, the diffraction peaks at 16.5°, 19.0°, 31.8°, 33.3°, 34.7°, and 37.4° corresponded to the final discharge product of cubic Na<sub>15</sub>Sn<sub>4</sub>. As shown in Figure 16(F), metallic Sn was transformed to cubic NaSn<sub>3</sub> and then orthorhombic NaSn in the initial Na<sup>+</sup> insertion process. Upon further sodiation, the rhombohedral Na<sub>9</sub>Sn<sub>4</sub> containing Sn-Sn dimers with a distance of 2.85 Å and five Na atoms oriented in the same direction was formed. Finally, cubic Na<sub>15</sub>Sn<sub>4</sub> was generated after full sodiation, in which an isolated Sn atom is surrounded by Na atoms in the relatively symmetric 12-fold coordination. In the reverse process, Na<sub>9</sub>Sn<sub>4</sub> was gradually desodiated to Sn with four distinctive plateaus of states E-I, as shown in Figure 16D and E. The diffraction peak of Cu<sub>6</sub>Sn<sub>5</sub> showed no change during cycling, which is indicative of its nonactivity in SIBs<sup>[163]</sup>. However, Cu<sub>6</sub>Sn<sub>5</sub> acted as a buffer layer to improve the electron conductivity between the active Sn and Cu foil. It was speculated that the reversible reactions of Sn were Sn ↔ NaSn<sub>3</sub> ↔ NaSn ↔ Na<sub>9</sub>Sn<sub>4</sub> ↔ Na<sub>15</sub>Sn<sub>4</sub>. Zhang *et al.* also observed other sodiation phases, such as NaSn, Na<sub>9</sub>Sn<sub>4</sub>, and Na<sub>15</sub>Sn<sub>4</sub>, by *in situ* XRD [Figure 16G]<sup>[164]</sup>.



**Figure 17.** (A) Cycling performance of Sb hollow spheres. (B) Rate performance of Sb hollow spheres. (C) Schematic of lithiation of Sb hollow spheres. Reproduced with permission<sup>[175]</sup> (Copyright 2014, American Chemical Society). (D) SEM of porous hollow Sb chains. (E) Cycling performance of porous hollow Sb chains and Sb/Gr. (F) Rate performance of porous hollow Sb chains and Sb/Gr. Reproduced with permission<sup>[176]</sup> (Copyright 2019, American Chemical Society).

### Sb-based porous structures for LIBs and SIBs

Sb has attracted significant attention as an anode material for LIBs and SIBs because of its high theoretical capacity [Tables 1 and 2], abundant resources, low cost, and environmental friendliness<sup>[165]</sup>. Moreover, Sb has high electrical conductivity, reliable ion diffusivity, and low volume expansion (200%) compared to Si. Sb anodes have a safer Li<sup>+</sup>/Na<sup>+</sup> insertion potential of ~0.5 V, which not only affords stable working voltages in batteries but also shuns the formation of lithium dendrites at low voltages. Sb with a 2D layered structure offers a desirable framework for fast lithium storage. However, the dense Sb still leads to structural fracturing and instability of the SEI layer on the surface of Sb during charging/discharging to accelerate capacity degradation. So far, efforts have been made to overcome these issues. Pore formation in Sb materials can shorten the diffusion length of Li<sup>+</sup> and Na<sup>+</sup> and accommodate the volume expansion to improve the electrochemical properties. Typical examples of porous Sb-based materials and their associated electrochemical properties are presented in Table 5<sup>[161,162,164,166-175]</sup>.

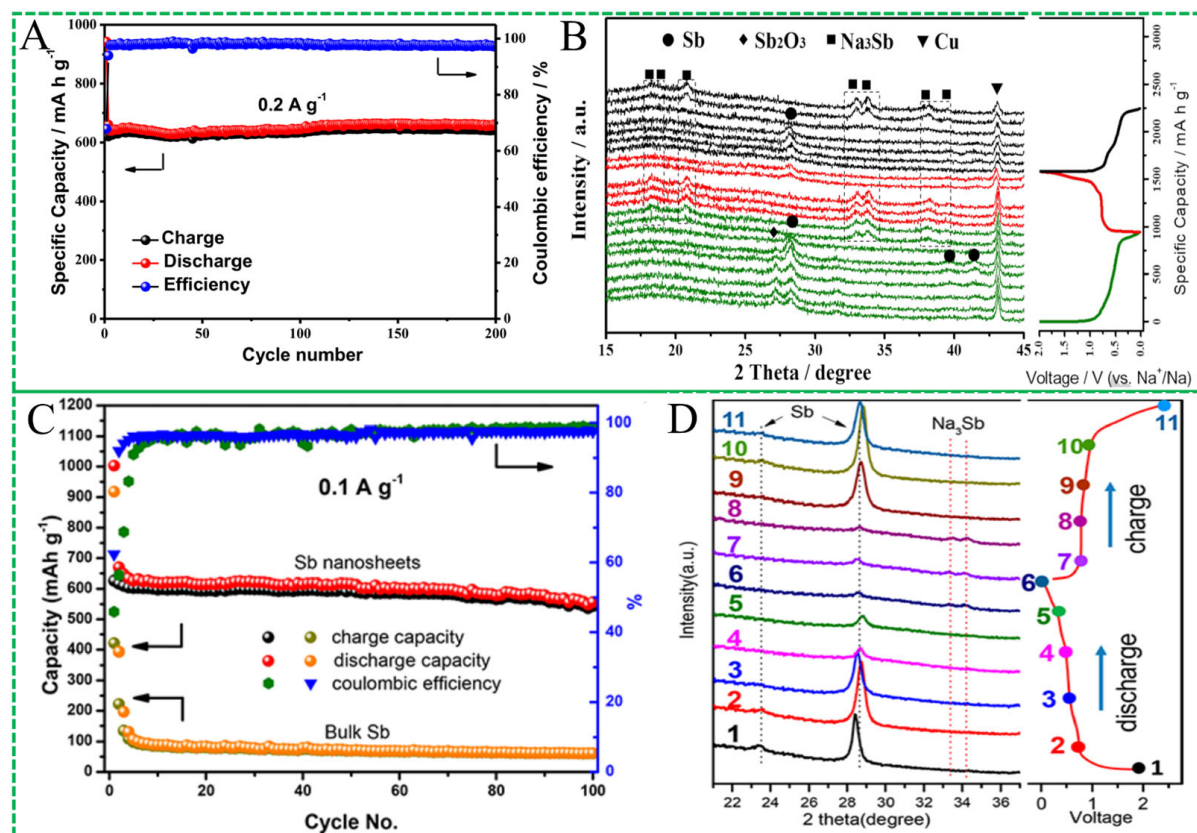
Hou *et al.* prepared porous hollow Sb spheres by a facile galvanic replacement method<sup>[175]</sup>. The hollow Sb spheres showed an initial specific capacity of 629.6 mAh g<sup>-1</sup> and retained a reversible capacity of 627.3 mAh g<sup>-1</sup> after 50 cycles at 100 mA g<sup>-1</sup>, corresponding to a capacity retention of 99.6% [Figure 17A]. In addition, such an electrode exhibited a high rate capacity of 435.6 mAh g<sup>-1</sup> at 1600 mA g<sup>-1</sup> [Figure 17B]. The superior electrochemical properties can be attributed to the unique hollow and porous spherical structure [Figure 17C]. The hollow Sb spheres adapted to the volume change and strain during Li<sup>+</sup> insertion and extraction, and the 3D Sb structure ensured efficient and continuous electron transportation. The large electrode/electrolyte contact area also provided many active centers for charge transfer to enhance the electrochemical kinetics. Rodriguez *et al.* synthesized 3D Sb chains with a rhombohedral phase by reduction [Figure 17D]<sup>[176]</sup>. The 3D Sb electrode exhibited excellent Li storage properties, as exemplified by a highly reversible capacity of 523 mAh g<sup>-1</sup> at 0.5 C after 100 cycles and a retention of 92% [Figure 17E]. Moreover,

these materials showed more stable rates and a high specific capacity of 430 mAh g<sup>-1</sup> at 1 C [Figure 17F]. The sodium storage performance of the 3D Sb chains was better than that of Sb/Gr due to the alleviated volume expansion. Meng and co-workers prepared porous Sb with 3D Sb dendrites by a galvanic replacement reaction between Sb<sup>3+</sup> and Zn powder<sup>[177]</sup>. The porous Sb with 3D dendrites showed a high initial charging capacity of 838.6 mAh g<sup>-1</sup> at 0.1 A g<sup>-1</sup>, corresponding to an ICE of 79.9% and a capacity retention of 603.2 mAh g<sup>-1</sup> after 124 cycles.

Hou *et al.* prepared porous hollow Sb microspheres (PHMSs) for SIBs using a replacement reaction employing Zn microspheres as the template<sup>[174]</sup>. The porous shell was metallic Sb and the inner core was a metallic Zn template. Hollow microspheres with porous shells were obtained after removing the Zn templates. The Sb PHMSs had a high initial charge capacity of 634.6 mAh g<sup>-1</sup> at a current density of 100 mA g<sup>-1</sup>, corresponding to an ICE of 64.6%. In addition, the Sb PHMSs exhibited a high reversible capacity of 617 mAh g<sup>-1</sup>, a retention of 97.2% after 100 cycles at 100 mA g<sup>-1</sup>, and excellent rate performance (312.9 mAh g<sup>-1</sup> at 3,200 mA g<sup>-1</sup>). The superior electrochemical characteristics stemmed from the unique porous and hollow structure of Sb PHMSs, which could accommodate the strain and facilitate Na<sup>+</sup> diffusion during repeated alloying/dealloying. Liu *et al.* studied the effects of the morphology of porous antimony (P-Sb) and the size of Sb particles on the electrochemical properties<sup>[173]</sup>. The coral-like P-Sb exhibited excellent electrochemical reversibility after 200 cycles at 100 mA g<sup>-1</sup>. The P-Sb electrode could be reversibly cycled at a high current density of 3,300 mA g<sup>-1</sup> and showed a high capacity of 420 mAh g<sup>-1</sup>, indicating the fast transfer of sodium ions and electrons. The P-Sb could adapt to the volume change of Na<sup>+</sup> insertion and improve the capacity retention. The high surface area of the pores allowed for efficient Na<sup>+</sup>/electron exchange to improve the capacity and cycling life of SIBs. The improvement rendered by the coral-like Sb anode arose mainly from the high porosity, and therefore a suitable porous structure plays an essential role in the electrochemical properties of Sb electrodes.

Ma *et al.* fabricated mesoporous antimony-based Sb<sub>2</sub>O<sub>3</sub>@Sb with an ultrafine bicontinuous mesoporous structure in the process of dealloying the Mg<sub>90</sub>Sb<sub>10</sub> precursor<sup>[172]</sup>. Sb<sub>2</sub>O<sub>3</sub>@Sb with a mesoporous structure exhibited an ultrahigh specific capacity of 659 mAh g<sup>-1</sup> at 0.2 A g<sup>-1</sup> and excellent cycling stability [Figure 18A]. *Operando* XRD measurements were executed to study the Na storage mechanism in the mesoporous Sb<sub>2</sub>O<sub>3</sub>@Sb electrode [Figure 18B]. At the beginning of the first discharge, only crystalline Sb<sub>2</sub>O<sub>3</sub> and Sb peaks could be observed. With the progress of the first discharge, the peak intensities of Sb<sub>2</sub>O<sub>3</sub> gradually decreased and disappeared, indicating the conversion reaction of Sb<sub>2</sub>O<sub>3</sub> with Na to form Na<sub>2</sub>O and Sb. In the later stage, the Sb peaks began to weaken and finally vanished. Moreover, the peak of Sb at 28.7° slightly shifted to lower 2θ angles, perhaps due to the insertion of Na into the Sb lattice at the early stage of sodiation. Afterwards, the well-defined crystalline peaks of hexagonal Na<sub>3</sub>Sb appeared in the final stage of the first discharge. In contrast, Li *et al.* reported multidimensional porous Sb nanostructures (Sb NS) synthesized by a facile chemical dealloying strategy<sup>[178]</sup>. Such Sb NS anodes exhibited a high reversible capacity of 620 mAh g<sup>-1</sup> and retained 90.2% capacity after 100 cycles at 100 mA g<sup>-1</sup> [Figure 18C]. An *ex situ* XRD analysis of the Sb-NS electrodes at different charge-discharge states was carried out to further understand the mechanisms of sodium storage [Figure 18D]. In the discharge process, the intensities of the Sb peaks gradually weakened and almost disappeared when the cell was fully discharged to 0.01 V. Moreover, new peaks of 33.5° and 34.3° appeared, corresponding to the formation of the Na<sub>3</sub>Sb phase, indicating the conversion reaction of Sb with Na to form Na<sub>3</sub>Sb. During the subsequent charge process, the Na<sub>3</sub>Sb peaks gradually disappeared, while the intensities of the Sb peaks increased, suggesting the transformation of Na<sub>3</sub>Sb into Sb.





**Figure 18.** (A) Cycling performance of  $\text{Sb}_2\text{O}_3@\text{Sb}$ . (B) Operando XRD patterns of mesoporous  $\text{Sb}_2\text{O}_3@\text{Sb}$  electrode. Reproduced with permission<sup>[172]</sup> (Copyright 2018, Elsevier). (C) Cycling performance of Sb-NS electrodes. (D) Ex situ XRD patterns of Sb-NS electrodes at different charge-discharge states. Reproduced with permission<sup>[178]</sup> (Copyright 2019, American Chemical Society).

## CONCLUSION AND OUTLOOK

Earth-abundant alloying materials (e.g., Si, Ge, Sn, and Sb) with high gravimetric and volumetric capacities have emerged as promising electrode materials to replace low-capacity carbonaceous anode materials in next-generation high energy density LIBs and SIBs. Nevertheless, the large volume change and unstable electrode interface of alloys impede their commercial development. Micro- or sub-microporous alloying materials comprised of nano-units can overcome some of these hurdles by combining the virtues of nano- and microscale materials. In this review, recent advances in porous microscale alloying materials are described from the perspective of high-capacity anodes in LIBs and SIBs. Porous alloys have remarkable properties in Li- and Na-ion storage by combining the structural advantages of nano- and micromaterials. Recent developments pertaining to the composition/structural design, modification, and mechanisms to improve the electron/ion conductivity and structural stability are discussed. Different fabrication methods, including dealloying, templating, chemical etching, and self-assembly, are summarized, and common alloying materials and their relevant properties for LIBs and SIBs are compared. Although significant progress has been made, the practical implementation of porous microscale alloys still faces some challenges.

First, the recognized evaluation parameters of porous structures and the quantitative relationship between the electrochemical characteristics and structures remain unclear. On the one hand, the porosity determines the tap density and internal space to accommodate volume expansion. Higher porosity results in a smaller volume expansion at the particle level but leads to a lower tap density and volumetric capacity of the active



materials and vice versa. On the other hand, the size and arrangement of the nano-units in the porous materials affect the active sites, Li- and Na-ion insertion distance, and mechanical stability of the active materials. Nano-ligaments with a smaller size are beneficial for Li- and Na-ion storage and transmission, but the mechanical strength of the framework may not be sufficient to endure the large stress during Li/Na alloying. The particle size determines the tap density and electron/ion distance of the active materials and is crucial to the optimization of the electrochemical properties. The various alloys have different properties. For instance, research into the alloys with high conductivity, such as Sn, Sb, and Bi, should focus on improving the electron conductivity, whereas that of other alloys, such as Si, need to balance the electron/ion conductivity. Overall, the quantitative assessment of the structural parameters must be improved, and the relationship with the structure of porous alloying anode materials must be better understood to expedite their application in LIBs and SIBs.

Second, large-scale and low-cost fabrication methods for different materials are highly desirable for LIBs and SIBs. Currently, porous alloys are prepared by chemical/noble-metal etching dealloying, liquid-metal dealloying, and templating. Chemical/electrochemical dealloying using an acidic solution to selectively dissolve one active metal component and leave another metallic ligament is one of the most common methods for porous alloys. However, this method is time-consuming and not suitable for active metals, and the parameters of bicontinuous metallic frameworks are difficult to control. The liquid metal dealloying method has problems, such as the high temperature, metal residues, and high cost rendering it to be not economical or sustainable. The template technique requires costly porous templates that are difficult to implement at a large scale. Although other methods, such as the gas dealloying of Mg<sub>2</sub>Si, have been used to obtain porous Si comprising nanoscale pores and metallic ligaments, the large-scale and low-cost fabrication of porous alloying materials with adjustable structures requires more research and development.

Third, issues, such as the mechanical stability and electrolyte absorption, affect the cycling lifetime of batteries. In the typical electrode production process, most of the high-capacity anodes, such as Si, should be mixed with commercial graphite particles, and the rolling procedure under tens of MPa pressure is essential to obtaining high-quality electrode films with a high tap density and surface evenness. The porous structure of alloys can be destroyed easily during ball milling with graphite and rolling of the electrode. Hence, optimizing the structural parameters to enhance the mechanical strength should be considered in practical applications. In contrast, the porous structure with a higher specific surface area and more pores consume more electrolytes, resulting in the nonuniform dispersion of electrolytes and more side reactions, which may produce inferior stability and raise safety concerns. Therefore, it is urgent to understand the relationship between electrolyte adsorption/consumption and materials properties, such as porosity.

Fourth, better comprehension of the phase/morphological evolution of materials at the atomic/molecular level and the failure mechanism of porous structures is crucial to the preparation and development of high-performance alloying electrodes. Although the results obtained by *in situ* characterization techniques are helpful in providing a better fundamental understanding, they are not sufficient to clearly explain how to improve the electrochemical properties of actual batteries. Furthermore, the formation mechanism and interfacial reactions of the SEI layers between alloying materials and electrolytes are still not well understood, and further research, including quantitative analysis, is necessary in order to fathom the effects of different materials under actual application conditions.

## DECLARATIONS

### Authors' contributions

Conceived the manuscript: Li G, Guo S, Gao B

Wrote the manuscript: Li G, Guo S, Gao B

Reviewed the manuscript: Gao B, Chu P, Huo K

Contributed to the discussion of the manuscript: Li G, Xiang B, Mei S, Guo S, Zheng Y, Zhang X, Gao B, Chu P, Huo K

### Availability of data and materials

Not applicable.

### Financial support and sponsorship

This work was financially supported by the National Natural Science Foundation of China (U2004210, 51974208, U2003130, 21875080, and 52002297), the Outstanding Youth Foundation of Natural Science Foundation of Hubei Province (2020CFA099), the Special Project of Central Government for Local Science and Technology Development of Hubei Province (2019ZYYD024), the Innovation group of Natural Science Foundation of Hubei Province (2019CFA020), and the City University of Hong Kong Strategic Research Grants (7005505).

### Conflicts of interest

All authors declared that there are no conflicts of interest.

### Ethical approval and consent to participate

Not applicable.

### Consent for publication

Not applicable.

### Copyright

© The Author(s) 2022.

## REFERENCES

1. Gogotsi Y, Simon P. Materials science. True performance metrics in electrochemical energy storage. *Science* 2011;334:917-8. [DOI](#) [PubMed](#)
2. Zu L, Zhang W, Qu L, et al. Mesoporous materials for electrochemical energy storage and conversion. *Adv Energy Mater* 2020;10:2002152. [DOI](#)
3. Jiang B, Li J, Luo B, et al. LiPO<sub>2</sub>F<sub>2</sub> electrolyte additive for high-performance Li-rich cathode material. *J Energy Chem* 2021;60:564-71. [DOI](#)
4. Cheng HM, Li F. Charge delivery goes the distance. *Science* 2017;356:582-3. [DOI](#) [PubMed](#)
5. Zhang Z, Zhang D, Lin H, Chen Y. Flexible fiber-shaped supercapacitors with high energy density based on self-twisted graphene fibers. *J Power Sources* 2019;433:226711. [DOI](#) [PubMed](#)
6. Pu X, Wang H, Zhao D, et al. Recent progress in rechargeable sodium-ion batteries: toward high-power applications. *Small* 2019;15:e1805427. [DOI](#) [PubMed](#)
7. Mishra K, Yadav N, Hashmi SA. Recent progress in electrode and electrolyte materials for flexible sodium-ion batteries. *J Mater Chem A* 2020;8:22507-43. [DOI](#)
8. Xu B, Qian D, Wang Z, Meng YS. Recent progress in cathode materials research for advanced lithium ion batteries. *Mater Sci Eng R Rep* 2012;73:51-65. [DOI](#)
9. Choi JU, Voronina N, Sun Y, Myung S. Recent progress and perspective of advanced high-energy Co-less Ni-rich cathodes for Li-ion batteries: yesterday, today, and tomorrow. *Adv Energy Mater* 2020;10:2002027. [DOI](#)
10. Zhai L, Li G, Yang X, et al. 30 Li<sup>+</sup>-accommodating covalent organic frameworks as ultralong cyclable high-capacity Li-ion battery electrodes. *Adv Funct Materials* 2022;32:2108798. [DOI](#)
11. Wang L, Światowska J, Dai S, et al. Promises and challenges of alloy-type and conversion-type anode materials for sodium-ion batteries. *Mater Today Energy* 2019;11:46-60. [DOI](#)
12. Zhang H, Hasa I, Passerini S. Beyond insertion for Na-ion batteries: nanostructured alloying and conversion anode materials. *Adv Energy Mater* 2018;8:1702582. [DOI](#)

13. Li X, Wang Y, Lv L, Zhu G, Qu Q, Zheng H. Electroactive organics as promising anode materials for rechargeable lithium ion and sodium ion batteries. *Energy Mater* 2022;2:200014. [DOI](#)
14. Zhao L, Hu Z, Lai W, et al. Hard carbon anodes: fundamental understanding and commercial perspectives for Na-ion batteries beyond Li-ion and K-ion counterparts. *Adv Energy Mater* 2021;11:2002704. [DOI](#)
15. Li G, Chen K, Wang Y, et al. Cream roll-inspired advanced MnS/C composite for sodium-ion batteries: encapsulating MnS cream into hollow N,S-co-doped carbon rolls. *Nanoscale* 2020;12:8493-501. [DOI](#) [PubMed](#)
16. Hou H, Qiu X, Wei W, Zhang Y, Ji X. Carbon anode materials for advanced sodium-ion batteries. *Adv Energy Mater* 2017;7:1602898. [DOI](#) [PubMed](#)
17. Chang H, Wu Y, Han X, Yi T. Recent developments in advanced anode materials for lithium-ion batteries. *Energy Mater* 2021. [DOI](#)
18. Cao L, Liang X, Ou X, et al. Heterointerface engineering of hierarchical Bi<sub>2</sub>S<sub>3</sub>/MoS<sub>2</sub> with self-generated rich phase boundaries for superior sodium storage performance. *Adv Funct Mater* 2020;30:1910732. [DOI](#)
19. Xiong X, Yang C, Wang G, et al. SnS nanoparticles electrostatically anchored on three-dimensional N-doped graphene as an active and durable anode for sodium-ion batteries. *Energy Environ Sci* 2017;10:1757-63. [DOI](#)
20. Yang C, Liang X, Ou X, et al. Heterostructured nanocube-shaped binary sulfide (SnCo)S<sub>2</sub> interlaced with S-doped graphene as a high-performance anode for advanced Na<sup>+</sup> batteries. *Adv Funct Mater* 2019;29:1807971. [DOI](#)
21. Ou X, Cao L, Liang X, et al. Fabrication of SnS<sub>2</sub>/Mn<sub>2</sub>SnS<sub>4</sub>/carbon heterostructures for sodium-ion batteries with high initial coulombic efficiency and cycling stability. *ACS Nano* 2019;13:3666-76. [DOI](#) [PubMed](#)
22. Chen K, Li G, Hu Z, et al. Simple preparation of baroque Mn-based chalcogenide/honeycomb-like carbon composites for sodium-ion batteries from renewable *Pleurotus Eryngii*. *Energy Fuels* ;35:6265-71. [DOI](#)
23. Wu C, Dou SX, Yu Y. The state and challenges of anode materials based on conversion reactions for sodium storage. *Small* 2018;14:e1703671. [DOI](#) [PubMed](#)
24. Lu Y, Yu L, Lou XW. Nanostructured conversion-type anode materials for advanced lithium-ion batteries. *Chem* 2018;4:972-96. [DOI](#)
25. Chae S, Ko M, Kim K, Ahn K, Cho J. Confronting issues of the practical implementation of Si anode in high-energy lithium-ion batteries. *Joule* 2017;1:47-60. [DOI](#)
26. Yang Z, Song Y, Zhang C, et al. Porous 3D silicon-diamondyne blooms excellent storage and diffusion properties for Li, Na, and K ions. *Adv Energy Mater* 2021;11:2101197. [DOI](#)
27. Ke C, Liu F, Zheng Z, et al. Boosting lithium storage performance of Si nanoparticles via thin carbon and nitrogen/phosphorus co-doped two-dimensional carbon sheet dual encapsulation. *Rare Met* 2021;40:1347-56. [DOI](#)
28. Cheng X, Shao R, Li D, et al. A self-healing volume variation three-dimensional continuous bulk porous bismuth for ultrafast sodium storage. *Adv Funct Mater* 2021;31:2011264. [DOI](#)
29. Lei K, Wang J, Chen C, et al. Recent progresses on alloy-based anodes for potassium-ion batteries. *Rare Met* 2020;39:989-1004. [DOI](#)
30. Imtiaz S, Amiin IS, Xu Y, Kennedy T, Blackman C, Ryan KM. Progress and perspectives on alloying-type anode materials for advanced potassium-ion batteries. *Mater Today* 2021;48:241-69. [DOI](#)
31. Niu J, Zhang Z, Aurbach D. Alloy anode materials for rechargeable Mg ion batteries. *Adv Energy Mater* 2020;10:2000697. [DOI](#) [PubMed](#)
32. Wu X, He G, Ding Y. Dealloyed nanoporous materials for rechargeable post-lithium batteries. *ChemSusChem* 2020;13:3287. [DOI](#) [PubMed](#)
33. Qi S, Deng J, Zhang W, Feng Y, Ma J. Recent advances in alloy-based anode materials for potassium ion batteries. *Rare Met* 2020;39:970-88. [DOI](#)
34. Chen Q, Ding Y, Chen M. Nanoporous metal by dealloying for electrochemical energy conversion and storage. *MRS Bull* 2018;43:43-8. [DOI](#)
35. Artymowicz D, Erlebacher J, Newman R. Relationship between the parting limit for de-alloying and a particular geometric high-density site percolation threshold. *Philos Mag* 2009;89:1663-93. [DOI](#)
36. Feng J, Zhang Z, Ci L, Zhai W, Ai Q, Xiong S. Chemical dealloying synthesis of porous silicon anchored by in situ generated graphene sheets as anode material for lithium-ion batteries. *J Power Sources* 2015;287:177-83. [DOI](#)
37. Zhang H, An W, Song H, et al. Synthesis of micro-sized porous antimony via vapor dealloying for high-performance Na-ion battery anode. *Solid State Ionics* 2020;352:115365. [DOI](#)
38. Sohn M, Lee DG, Park H, Park C, Choi J, Kim H. Microstructure controlled porous silicon particles as a high capacity lithium storage material via dual step pore engineering. *Adv Funct Mater* 2018;28:1800855. [DOI](#)
39. Lin N, Li T, Han Y, Zhang Q, Xu T, Qian Y. Mesoporous hollow Ge microspheres prepared via molten-salt metallothermic reaction for high-performance Li-storage anode. *ACS Appl Mater Interfaces* 2018;10:8399-404. [DOI](#) [PubMed](#)
40. Yang Y, Liu S, Bian X, Feng J, An Y, Yuan C. Morphology- and porosity-tunable synthesis of 3D nanoporous SiGe alloy as a high-performance lithium-ion battery anode. *ACS Nano* 2018;12:2900-8. [DOI](#) [PubMed](#)
41. Gao H, Niu J, Zhang C, Peng Z, Zhang Z. A dealloying synthetic strategy for nanoporous bismuth-antimony anodes for sodium ion batteries. *ACS Nano* 2018;12:3568-77. [DOI](#) [PubMed](#)
42. Yan Y, Shi Y, Wang Z, Qin C, Zhang Y. AlF<sub>3</sub> microrods modified nanoporous Ge/Ag anodes fabricated by one-step dealloying strategy for stable lithium storage. *Mater Letters* 2020;276:128254. [DOI](#)

43. Ma W, Yin K, Gao H, Niu J, Peng Z, Zhang Z. Alloying boosting superior sodium storage performance in nanoporous tin-antimony alloy anode for sodium ion batteries. *Nano Energy* 2018;54:349-59. DOI
44. Zhang H, Zhang M, Zhang M, et al. Hybrid aerogel-derived Sn-Ni alloy immobilized within porous carbon/graphene dual matrices for high-performance lithium storage. *J Colloid Interface Sci* 2017;501:267-72. DOI PubMed
45. Yin H, Xiao W, Mao X, Zhu H, Wang D. Preparation of a porous nanostructured germanium from GeO<sub>2</sub> via a “reduction-alloying-dealloying” approach. *J Mater Chem A* 2015;3:1427-30. DOI
46. Yuan Y, Xiao W, Wang Z, Fray DJ, Jin X. Efficient nanostructuring of silicon by electrochemical alloying/dealloying in molten salts for improved lithium storage. *Angew Chem Int Ed Engl* 2018;57:15743-8. DOI PubMed
47. Wada T, Ichitsubo T, Yubuta K, Segawa H, Yoshida H, Kato H. Bulk-nanoporous-silicon negative electrode with extremely high cyclability for lithium-ion batteries prepared using a top-down process. *Nano Lett* 2014;14:4505-10. DOI PubMed
48. Wada T, Yamada J, Kato H. Preparation of three-dimensional nanoporous Si using dealloying by metallic melt and application as a lithium-ion rechargeable battery negative electrode. *J Power Sources* 2016;306:8-16. DOI
49. Chen Y, Yuan Y, Xu C, et al. Multi-step low-cost synthesis of ultrafine silicon porous structures for high-reversible lithium-ion battery anodes. *J Mater Sci* 2020;55:13938-50. DOI
50. Wang J, Huang W, Kim YS, et al. Scalable synthesis of nanoporous silicon microparticles for highly cyclable lithium-ion batteries. *Nano Res* 2020;13:1558-63. DOI
51. An W, Gao B, Mei S, et al. Scalable synthesis of ant-nest-like bulk porous silicon for high-performance lithium-ion battery anodes. *Nat Commun* 2019;10:1447. DOI PubMed PMC
52. An Y, Tian Y, Wei H, et al. Porosity- and graphitization-controlled fabrication of nanoporous silicon@carbon for lithium storage and its conjugation with MXene for lithium-metal anode. *Adv Funct Mater* 2019;30:1908721. DOI
53. Míguez H, Meseguer F, López C, et al. Germanium FCC structure from a colloidal crystal template. *Langmuir* 2000;16:4405-8. DOI
54. Song T, Jeon Y, Samal M, et al. A Ge inverse opal with porous walls as an anode for lithium ion batteries. *Energy Environ Sci* 2012;5:9028. DOI
55. Geier S, Jung R, Peters K, Gasteiger HA, Fattakhova-rohlfing D, Fässler TF. A wet-chemical route for macroporous inverse opal Ge anodes for lithium ion batteries with high capacity retention. *Sustainable Energy Fuels* 2018;2:85-90. DOI
56. Esmanski A, Ozin GA. Silicon inverse-opal-based macroporous materials as negative electrodes for lithium ion batteries. *Adv Funct Mater* 2009;19:1999-2010. DOI
57. Jeong J, Kim K, Jung D, Kim K, Lee S, Oh E. High-performance characteristics of silicon inverse opal synthesized by the simple magnesium reduction as anodes for lithium-ion batteries. *J Power Sources* 2015;300:182-9. DOI
58. Gowda SR, Pushparaj V, Herle S, et al. Three-dimensionally engineered porous silicon electrodes for Li-ion batteries. *Nano Lett* 2012;12:6060-5. DOI PubMed
59. Bao Z, Weatherspoon MR, Shian S, et al. Chemical reduction of three-dimensional silica micro-assemblies into microporous silicon replicas. *Nature* 2007;446:172-5. DOI PubMed
60. Hwa Y, Kim W, Yu B, Hong S, Sohn H. Mesoporous nano-Si anode for Li-ion batteries produced by magnesio-mechanochemical reduction of amorphous SiO<sub>2</sub>. *Energy Technol* 2013;1:327-31. DOI
61. Wang B, Li W, Wu T, Guo J, Wen Z. Self-template construction of mesoporous silicon submicrocube anode for advanced lithium ion batteries. *Energy Stor Mater* 2018;15:139-47. DOI
62. Entwistle J, Rennie A, Patwardhan S. A review of magnesiothermic reduction of silica to porous silicon for lithium-ion battery applications and beyond. *J Mater Chem A* 2018;6:18344-56. DOI
63. Jia H, Kloepsch R, He X, et al. Reversible storage of lithium in three-dimensional macroporous germanium. *Chem Mater* 2014;26:5683-8. DOI
64. Lin N, Han Y, Zhou J, et al. A low temperature molten salt process for aluminothermic reduction of silicon oxides to crystalline Si for Li-ion batteries. *Energy Environ Sci* 2015;8:3187-91. DOI
65. Manukyan KV, Schools RS, Mukasyan AS. Size-tunable germanium particles prepared by self-sustaining reduction of germanium oxide. *J Solid State Chem* 2019;270:92-7. DOI
66. Peterson AK, Morgan DG, Skrabalak SE. Aerosol synthesis of porous particles using simple salts as a pore template. *Langmuir* 2010;26:8804-9. DOI PubMed
67. Dai F, Zai J, Yi R, et al. Bottom-up synthesis of high surface area mesoporous crystalline silicon and evaluation of its hydrogen evolution performance. *Nat Commun* 2014;5:3605. DOI PubMed
68. Tang D, Yu H, Zhao J, et al. Bottom-up synthesis of mesoporous germanium as anodes for lithium-ion batteries. *J Colloid Interface Sci* 2020;561:494-500. DOI PubMed
69. Ge M, Fang X, Rong J, Zhou C. Review of porous silicon preparation and its application for lithium-ion battery anodes. *Nanotechnology* 2013;24:422001. DOI PubMed
70. Huang Z, Geyer N, Werner P, de Boor J, Gösele U. Metal-assisted chemical etching of silicon: a review. *Adv Mater* 2011;23:285-308. DOI PubMed
71. Peng K, Wu Y, Fang H, Zhong X, Xu Y, Zhu J. Uniform, Axial-orientation alignment of one-dimensional single-crystal silicon nanostructure arrays. *Angew Chem* 2005;117:2797-802. DOI PubMed
72. Li X, Yan C, Wang J, et al. Stable silicon anodes for lithium-ion batteries using mesoporous metallurgical silicon. *Adv Energy Mater* 2015;5:1401556. DOI



73. Bai F, Li M, Song D, Yu H, Jiang B, Li Y. One-step synthesis of lightly doped porous silicon nanowires in HF/AgNO<sub>3</sub>/H<sub>2</sub>O<sub>2</sub> solution at room temperature. *J Solid State Chem* 2012;196:596-600. DOI
74. Hochbaum AI, Gargas D, Hwang YJ, Yang P. Single crystalline mesoporous silicon nanowires. *Nano Lett* 2009;9:3550-4. DOI PubMed
75. Zhong X, Qu Y, Lin YC, Liao L, Duan X. Unveiling the formation pathway of single crystalline porous silicon nanowires. *ACS Appl Mater Interfaces* 2011;3:261-70. DOI PubMed PMC
76. Zhang Z, Wang Y, Ren W, Tan Q, Zhong Z, Su F. Low-cost synthesis of porous silicon via ferrite-assisted chemical etching and their application as Si-based anodes for Li-ion batteries. *Adv Electron Mater* 2015;1:1400059. DOI
77. Cao M, Li SY, Deng JX, et al. Preparation of large-area porous silicon through Cu-assisted chemical etching. *MSF* 2016;847:78-83. DOI
78. Rezvani SJ, Pinto N, Boarino L. Rapid formation of single crystalline Ge nanowires by anodic metal assisted etching. *Cryst Eng Comm* 2016;18:7843-8. DOI
79. Han X, Zhang Z, Chen H, et al. Bulk boron doping and surface carbon coating enabling fast-charging and stable Si anodes: from thin film to thick Si electrodes. *J Mater Chem A* 2021;9:3628-36. DOI
80. Uhler A. Electrolytic shaping of germanium and Silicon. *Bell Syst Tech J* 1956;35:333-47. DOI
81. Thakur M, Sinsabaugh SL, Isaacson MJ, Wong MS, Biswal SL. Inexpensive method for producing macroporous silicon particulates (MPSPs) with pyrolyzed polyacrylonitrile for lithium ion batteries. *Sci Rep* 2012;2:795. DOI PubMed PMC
82. Turner DR. Electropolishing silicon in hydrofluoric acid solutions. *J Electrochem Soc* 1958;105:402. DOI
83. Bioud YA, Boucherif A, Belarouci A, et al. Fast growth synthesis of mesoporous germanium films by high frequency bipolar electrochemical etching. *Electrochim Acta* 2017;232:422-30. DOI
84. Bang BM, Kim H, Lee J, Cho J, Park S. Mass production of uniform-sized nanoporous silicon nanowire anodes via block copolymer lithography. *Energy Environ Sci* 2011;4:3395. DOI
85. Jia H, Zheng J, Song J, et al. A novel approach to synthesize micrometer-sized porous silicon as a high performance anode for lithium-ion batteries. *Nano Energy* 2018;50:589-97. DOI
86. Jeong YK, Huang W, Vilá RA, et al. Microclusters of kinked silicon nanowires synthesized by a recyclable iodide process for high-performance lithium-ion battery anodes. *Adv Energy Mater* 2020;10:2002108. DOI
87. Jia H, Li X, Song J, et al. Hierarchical porous silicon structures with extraordinary mechanical strength as high-performance lithium-ion battery anodes. *Nat Commun* 2020;11:1474. DOI PubMed PMC
88. Yao R, Xie L, Wu Y, Meng W, He Y, Zhao D. Controllable self-assembled mesoporous silicon nanocrystals framework as anode material for Li-ion battery. *Electrochim Acta* 2021;390:138850. DOI
89. Liu X, Giordano C, Antonietti M. A molten-salt route for synthesis of Si and Ge nanoparticles: chemical reduction of oxides by electrons solvated in salt melt. *J Mater Chem* 2012;22:5454. DOI
90. Xiang B, An W, Fu J, et al. Graphene-encapsulated blackberry-like porous silicon nanospheres prepared by modest magnesiothermic reduction for high-performance lithium-ion battery anode. *Rare Met* 2021;40:383-92. DOI
91. Chevrier VL, Zwanziger JW, Dahn JR. First principles studies of silicon as a negative electrode material for lithium-ion batteries. *Can J Phys* 2009;87:625-32. DOI
92. Shenoy V, Johari P, Qi Y. Elastic softening of amorphous and crystalline Li-Si Phases with increasing Li concentration: a first-principles study. *J Power Sources* 2010;195:6825-30. DOI
93. Zuo X, Zhu J, Müller-buschbaum P, Cheng Y. Silicon based lithium-ion battery anodes: a chronicle perspective review. *Nano Energy* 2017;31:113-43. DOI
94. Shen L, Guo X, Fang X, Wang Z, Chen L. Magnesiothermally reduced diatomaceous earth as a porous silicon anode material for lithium ion batteries. *J Power Sources* 2012;213:229-32. DOI
95. Mu T, Shen B, Lou S, et al. Scalable mesoporous silicon microparticles composed of interconnected nanoplates for superior lithium storage. *Chem Eng J* 2019;375:121923. DOI
96. He W, Tian H, Xin F, Han W. Scalable fabrication of micro-sized bulk porous Si from Fe-Si alloy as a high performance anode for lithium-ion batteries. *J Mater Chem A* 2015;3:17956-62. DOI
97. Han X, Zhang Z, Zheng G, et al. Scalable engineering of bulk porous Si anodes for high initial efficiency and high-areal-capacity lithium-ion batteries. *ACS Appl Mater Interfaces* 2019;11:714-21. DOI PubMed
98. Jia H, Gao P, Yang J, Wang J, Nuli Y, Yang Z. Novel three-dimensional mesoporous silicon for high power lithium-ion battery anode material. *Adv Energy Mater* 2011;1:1036-9. DOI
99. Zhou Y, Jiang X, Chen L, et al. Novel mesoporous silicon nanorod as an anode material for lithium ion batteries. *Electrochim Acta* 2014;127:252-8. DOI
100. Tang J, Yin Q, Wang Q, et al. Two-dimensional porous silicon nanosheets as anode materials for high performance lithium-ion batteries. *Nanoscale* 2019;11:10984-91. DOI PubMed
101. Bang BM, Lee J, Kim H, Cho J, Park S. High-performance macroporous bulk silicon anodes synthesized by template-free chemical etching. *Adv Energy Mater* 2012;2:878-83. DOI
102. Li X, Gu M, Hu S, et al. Mesoporous silicon sponge as an anti-pulverization structure for high-performance lithium-ion battery anodes. *Nat Commun* 2014;5:4105. DOI PubMed
103. Zhang Z, Wang Y, Ren W, et al. Scalable synthesis of interconnected porous silicon/carbon composites by the rochow reaction as

- high-performance anodes of lithium ion batteries. *Angew Chem* 2014;126:5265-9. DOI PubMed
104. Zhong H, Zhan H, Zhou Y. Synthesis of nanosized mesoporous silicon by magnesium-thermal method used as anode material for lithium ion battery. *J Power Sources* 2014;262:10-4. DOI
  105. Choi S, Bok T, Ryu J, Lee J, Cho J, Park S. Revisit of metallothermic reduction for macroporous Si: compromise between capacity and volume expansion for practical Li-ion battery. *Nano Energy* 2015;12:161-8. DOI
  106. Liang J, Li X, Hou Z, Guo C, Zhu Y, Qian Y. Nanoporous silicon prepared through air-oxidation demagnesium of Mg<sub>2</sub>Si and properties of its lithium ion batteries. *Chem Commun (Camb)* 2015;51:7230-3. DOI PubMed
  107. Jiang T, Zhang R, Yin Q, et al. Morphology, composition and electrochemistry of a nano-porous silicon versus bulk silicon anode for lithium-ion batteries. *J Mater Sci* 2017;52:3670-7. DOI
  108. Liu X, Miao R, Yang J, et al. Scalable and cost-effective preparation of hierarchical porous silicon with a high conversion yield for superior lithium-ion storage. *Energy Technol* 2016;4:593-9. DOI
  109. Jia H, Gao P, Yang J, Wang J, Nuli Y, Yang Z. Novel three-dimensional mesoporous silicon for high power lithium-ion battery anode material. *Adv Energy Mater* 2011;1:1036-9. DOI
  110. Xu Z, Gang Y, Garakani MA, Abouali S, Huang J, Kim J. Carbon-coated mesoporous silicon microsphere anodes with greatly reduced volume expansion. *J Mater Chem A* 2016;4:6098-106. DOI
  111. Kim Y, Lee J, Kim H. Nanoporous silicon flakes as anode active material for lithium-ion batteries. *Physica E Low Dimens Syst Nanostruct* 2017;85:223-6. DOI
  112. Kim N, Park H, Yoon N, Lee JK. Zeolite-templated mesoporous silicon particles for advanced lithium-ion battery anodes. *ACS Nano* 2018;12:3853-64. DOI PubMed
  113. Wang F, Zhao B, Zi W, Du H. Ionothermal synthesis of crystalline nanoporous silicon and its use as anode materials in lithium-ion batteries. *Nanoscale Res Lett* 2019;14:196. DOI PubMed PMC
  114. Yang Z, Du Y, Hou G, Ouyang Y, Ding F, Yuan F. Nanoporous silicon spheres preparation via a controllable magnesiothermic reduction as anode for Li-ion batteries. *Electrochim Acta* 2020;329:135141. DOI
  115. Sun X, Huang H, Chu K, Zhuang Y. Anodized macroporous silicon anode for integration of lithium-ion batteries on chips. *J Elec Mater* 2012;41:2369-75. DOI
  116. Wang F, Sun L, Zi W, Zhao B, Du H. Solution synthesis of porous silicon particles as an anode material for lithium ion batteries. *Chemistry* 2019;25:9071-7. DOI PubMed
  117. Wada T, Kato H. Preparation of nanoporous Si by dealloying in metallic melt and its application for negative electrode of lithium ion battery. *Mater Today: Proc* 2017;4:11465-9. DOI
  118. Ge M, Lu Y, Ercius P, et al. Large-scale fabrication, 3D tomography, and lithium-ion battery application of porous silicon. *Nano Lett* 2014;14:261-8. DOI PubMed
  119. Gao P, Tang H, Xing A, Bao Z. Porous silicon from the magnesiothermic reaction as a high-performance anode material for lithium ion battery applications. *Electrochim Acta* 2017;228:545-52. DOI
  120. Chen X, Bi Q, Sajjad M, et al. One-dimensional porous silicon nanowires with large surface area for fast charge-discharge lithium-ion batteries. *Nanomaterials (Basel)* 2018;8:285. DOI PubMed PMC
  121. Guo R, Zhang S, Ying H, Yang W, Wang J, Han WQ. New, Effective, and low-cost dual-functional binder for porous silicon anodes in lithium-ion batteries. *ACS Appl Mater Interfaces* 2019;11:14051-8. DOI PubMed
  122. Wang W, Favors Z, Ionescu R, et al. Monodisperse porous silicon spheres as anode materials for lithium ion batteries. *Sci Rep* 2015;5:8781. DOI PubMed PMC
  123. Pathak AD, Chanda UK, Samanta K, Mandal A, Sahu KK, Pati S. Selective leaching of Al from hypereutectic Al-Si alloy to produce nano-porous silicon (NPS) anodes for lithium ion batteries. *Electrochim Acta* 2019;317:654-62. DOI
  124. Entwistle JE, Patwardhan SV. Enabling scale-up of mesoporous silicon for lithium-ion batteries: a systematic study of a thermal moderator. *RSC Adv* 2021;11:3801-7. DOI PubMed PMC
  125. Zeng Y, Huang Y, Liu N, et al. N-doped porous carbon nanofibers sheathed pumpkin-like Si/C composites as free-standing anodes for lithium-ion batteries. *J Energy Chem* 2021;54:727-35. DOI
  126. Shen C, Ge M, Luo L, et al. In situ and ex situ TEM study of lithiation behaviours of porous silicon nanostructures. *Sci Rep* 2016;6:31334. DOI PubMed PMC
  127. Liu N, Lu Z, Zhao J, et al. A pomegranate-inspired nanoscale design for large-volume-change lithium battery anodes. *Nat Nanotechnol* 2014;9:187-92. DOI PubMed
  128. Shi J, Zu L, Gao H, Hu G, Zhang Q. Silicon-based self-assemblies for high volumetric capacity Li-ion batteries via effective stress management. *Adv Funct Mater* 2020;30:2002980. DOI
  129. Choi JH, Kim HK, Jin EM, et al. Facile and scalable synthesis of silicon nanowires from waste rice husk silica by the molten salt process. *J Hazard Mater* 2020;399:122949. DOI PubMed
  130. Kim H, Han B, Choo J, Cho J. Three-dimensional porous silicon particles for use in high-performance lithium secondary batteries. *Angew Chem* 2008;120:10305-8. DOI PubMed
  131. Tao Y, Zeng G, Xiao C, Liu Y, Qian Y, Feng J. Porosity controlled synthesis of nanoporous silicon by chemical dealloying as anode for high energy lithium-ion batteries. *J Colloid Interface Sci* 2019;554:674-81. DOI PubMed
  132. Wang J, Liao L, Lee HR, et al. Surface-engineered mesoporous silicon microparticles as high-Coulombic-efficiency anodes for lithium-ion batteries. *Nano Energy* 2019;61:404-10. DOI

133. Morito H, Yamada T, Ikeda T, Yamane H. Na-Si binary phase diagram and solution growth of silicon crystals. *J Alloys and Compd* 2009;480:723-6. [DOI](#)
134. Xu Y, Swaans E, Basak S, Zandbergen HW, Borsa DM, Mulder FM. Reversible Na-ion uptake in Si nanoparticles. *Adv Energy Mater* 2016;6:1501436. [DOI](#)
135. Han Y, Lin N, Xu T, et al. An amorphous Si material with a sponge-like structure as an anode for Li-ion and Na-ion batteries. *Nanoscale* 2018;10:3153-8. [DOI](#) [PubMed](#)
136. Lim C, Huang T, Shao P, et al. Experimental study on sodiation of amorphous silicon for use as sodium-ion battery anode. *Electrochim Acta* 2016;211:265-72. [DOI](#)
137. Qiu DF, Ma X, Zhang JD, Lin ZX, Zhao B. Mesoporous silicon microspheres produced from in situ magnesiothermic reduction of silicon oxide for high-performance anode material in sodium-ion batteries. *Nanoscale Res Lett* 2018;13:275. [DOI](#) [PubMed](#) [PMC](#)
138. Du FH, Li B, Fu W, Xiong YJ, Wang KX, Chen JS. Surface binding of polypyrrole on porous silicon hollow nanospheres for Li-ion battery anodes with high structure stability. *Adv Mater* 2014;26:6145-50. [DOI](#) [PubMed](#)
139. Yi Z, Lin N, Zhao Y, et al. A flexible micro/nanostructured Si microsphere cross-linked by highly-elastic carbon nanotubes toward enhanced lithium ion battery anodes. *Energy Stor Mater* 2019;17:93-100. [DOI](#)
140. Son Y, Kim N, Lee T, et al. Calendering-compatible macroporous architecture for silicon-graphite composite toward high-energy lithium-ion batteries. *Adv Mater* 2020;32:e2003286. [DOI](#) [PubMed](#)
141. Park MH, Kim K, Kim J, Cho J. Flexible dimensional control of high-capacity Li-ion-battery anodes: from 0D hollow to 3D porous germanium nanoparticle assemblies. *Adv Mater* 2010;22:415-8. [DOI](#) [PubMed](#)
142. Yang L, Gao Q, Li L, Tang Y, Wu Y. Mesoporous germanium as anode material of high capacity and good cycling prepared by a mechanochemical reaction. *Electrochem Commun* 2010;12:418-21. [DOI](#)
143. Ke FS, Mishra K, Jamison L, et al. Tailoring nanostructures in micrometer size germanium particles to improve their performance as an anode for lithium ion batteries. *Chem Commun (Camb)* 2014;50:3713-5. [DOI](#) [PubMed](#)
144. Liang J, Li X, Hou Z, et al. Honeycomb-like macro-germanium as high-capacity anodes for lithium-ion batteries with good cycling and rate performance. *Chem Mater* 2015;27:4156-64. [DOI](#)
145. Yoon T, Song G, Harzandi A, et al. Intramolecular deformation of zeotype-borogermanate toward a three-dimensional porous germanium anode for high-rate lithium storage. *J Mater Chem A* 2018;6:15961-7. [DOI](#)
146. Kwon D, Ryu J, Shin M, et al. Synthesis of dual porous structured germanium anodes with exceptional lithium-ion storage performance. *J Power Sources* 2018;374:217-24. [DOI](#)
147. Choi S, Kim J, Choi NS, Kim MG, Park S. Cost-effective scalable synthesis of mesoporous germanium particles via a redox-transmetalation reaction for high-performance energy storage devices. *ACS Nano* 2015;9:2203-12. [DOI](#) [PubMed](#)
148. Zhang C, Lin Z, Yang Z, et al. Hierarchically designed germanium microcubes with high initial coulombic efficiency toward highly reversible lithium storage. *Chem Mater* 2015;27:2189-94. [DOI](#)
149. Liu X, Lin N, Cai W, et al. Mesoporous germanium nanoparticles synthesized in molten zinc chloride at low temperature as a high-performance anode for lithium-ion batteries. *Dalton Trans* 2018;47:7402-6. [DOI](#) [PubMed](#)
150. Choi S, Cho YG, Kim J, et al. Mesoporous germanium anode materials for lithium-ion battery with exceptional cycling stability in wide temperature range. *Small* 2017;13:1603045. [DOI](#) [PubMed](#)
151. Mishra K, Liu X, Ke F, Zhou X. Porous germanium enabled high areal capacity anode for lithium-ion batteries. *Compos B Eng* 2019;163:158-64. [DOI](#)
152. Sosa AN, González I, Trejo A, Miranda Á, Salazar F, Cruz-Irisson M. Effects of lithium on the electronic properties of porous Ge as anode material for batteries. *J Comput Chem* 2020;41:2653-62. [DOI](#) [PubMed](#)
153. Kohandehghan A, Cui K, Kupsta M, et al. Activation with Li enables facile sodium storage in germanium. *Nano Lett* 2014;14:5873-82. [DOI](#) [PubMed](#)
154. Lu X, Adkins ER, He Y, et al. Germanium as a sodium ion battery material: in situ TEM reveals fast sodiation kinetics with high capacity. *Chem Mater* 2016;28:1236-42. [DOI](#)
155. Li M, Wang Z, Fu J, Ma K, Detsi E. In situ electrochemical dilatometry study of capacity fading in nanoporous Ge-based Na-ion battery anodes. *Scr Mater* 2019;164:52-6. [DOI](#)
156. Yi Z, Lin N, Li T, Han Y, Li Y, Qian Y. Meso-porous amorphous Ge: synthesis and mechanism of an anode material for Na and K storage. *Nano Res* 2019;12:1824-30. [DOI](#)
157. Song T, Yan M, Qian M. A dealloying approach to synthesizing micro-sized porous tin (Sn) from immiscible alloy systems for potential lithium-ion battery anode applications. *J Porous Mater* 2015;22:713-9. [DOI](#)
158. Ryu S, Shim HC, Song JT, et al. High-pressure evaporation-based nanoporous black Sn for enhanced performance of lithium-ion battery anodes. *Part Part Syst Charact* 2019;36:1800331. [DOI](#)
159. Cook JB, Detsi E, Liu Y, et al. Nanoporous tin with a granular hierarchical ligament morphology as a highly stable Li-ion battery anode. *ACS Appl Mater Interfaces* 2017;9:293-303. [DOI](#) [PubMed](#)
160. Wang JW, Liu XH, Mao SX, Huang JY. Microstructural evolution of tin nanoparticles during in situ sodium insertion and extraction. *Nano Lett* 2012;12:5897-902. [DOI](#) [PubMed](#)
161. Kim C, Lee K, Kim I, et al. Long-term cycling stability of porous Sn anode for sodium-ion batteries. *J Power Sources* 2016;317:153-8. [DOI](#)
162. Wang L, Ni Y, Lei K, Dong H, Tian S, Li F. 3D porous tin created by tuning the redox potential acts as an advanced electrode for

- sodium-ion batteries. *Chem Sus Chem* 2018;11:3376-81. DOI PubMed
163. Kim IT, Allcorn E, Manthiram A. Cu<sub>6</sub>Sn<sub>5</sub>-TiC-C nanocomposite anodes for high-performance sodium-ion batteries. *J Power Sources* 2015;281:11-7. DOI PubMed
  164. Zhang B, Rousse G, Foix D, Dugas R, Corte DA, Tarascon JM. Microsized Sn as advanced anodes in glyme-based electrolyte for Na-ion batteries. *Adv Mater* 2016;28:9824-30. DOI PubMed
  165. Liang S, Cheng Y, Zhu J, Xia Y, Müller-buschbaum P. A chronicle review of nonsilicon (Sn, Sb, Ge)-based lithium/sodium-ion battery alloying anodes. *Small Methods* 2020;4:2000218. DOI
  166. Detsi E, Petrisans X, Yan Y, et al. Tuning ligament shape in dealloyed nanoporous tin and the impact of nanoscale morphology on its applications in Na-ion alloy battery anodes. *Phys Rev Materials* 2018;2. DOI
  167. Guo M, Meng W, Zhang X, et al. Electrochemical behavior and self-organization of porous Sn nanocrystals@acetylene black microspheres in lithium-ion half cells. *Appl Surf Sci* 2019;470:36-43. DOI
  168. Cheng Y, Huang J, Li R, et al. Enhanced cycling performances of hollow Sn compared to solid Sn in Na-ion battery. *Electrochim Acta* 2015;180:227-33. DOI
  169. Shi L, Wang W. Synthesis and sodium storage performance of Sb porous nanostructure. *J Alloys Compd* 2020;846:156369. DOI
  170. Li M, Qiu T, Foucher AC, et al. Impact of hierarchical nanoporous architectures on sodium storage in antimony-based sodium-ion battery anodes. *ACS Appl Energy Mater* 2020;3:11231-41. DOI
  171. Yuan Y, Jan S, Wang Z, Jin X. A simple synthesis of nanoporous Sb/C with high Sb content and dispersity as an advanced anode for sodium ion batteries. *J Mater Chem A* 2018;6:5555-9. DOI
  172. Ma W, Wang J, Gao H, et al. A mesoporous antimony-based nanocomposite for advanced sodium ion batteries. *Energy Stor Mater* 2018;13:247-56. DOI
  173. Liu S, Feng J, Bian X, Liu J, Xu H. The morphology-controlled synthesis of a nanoporous-antimony anode for high-performance sodium-ion batteries. *Energy Environ Sci* 2016;9:1229-36. DOI
  174. Hou H, Jing M, Yang Y, et al. Sb porous hollow microspheres as advanced anode materials for sodium-ion batteries. *J Mater Chem A* 2015;3:2971-7. DOI
  175. Hou H, Jing M, Yang Y, Zhu Y, Fang L, Song W, Pan C, Yang X, Ji X. Sodium/lithium storage behavior of antimony hollow nanospheres for rechargeable batteries. *ACS Appl Mater Interfaces* 2014;6:16189-96. DOI PubMed
  176. Rodriguez JR, Hamann HJ, Mitchell GM, Ortalan V, Pol VG, Ramachandran PV. Three-Dimensional Antimony Nanochains for Lithium-Ion Storage. *ACS Appl Nano Mater* 2019;2:5351-5. DOI
  177. Meng W, Guo M, Chen J, Li D, Wang Z, Yang F. Porous Sb with three-dimensional Sb nanodendrites as electrode material for high-performance Li/Na-ion batteries. *Nanotechnology* 2020;31:175401. DOI PubMed
  178. Li H, Wang K, Zhou M, et al. Facile Tailoring of Multidimensional Nanostructured Sb for Sodium Storage Applications. *ACS Nano* 2019;13:9533-40. DOI PubMed